International Journal of Fatigue 177 (2023) 107931

Contents lists available at ScienceDirect

International Journal of Fatigue

journal homepage: www.elsevier.com/locate/ijfatigue

High and low cycle fatigue properties of selective laser melted AISI 316L and AlSi10Mg

Franco Concli [a], Riccardo Gerosa [b], Davide Panzeri [b,*], Lorenzo Fraccaroli [a]

[a] Faculty of Science and Technology, Free Universiy of Bolzano/Bozen, 39100 Bolzano, Italy
[b] Politecnico di Milano, Dipartimento di Meccanica, via La Masa 1, 20156 Milano, Italy

ARTICLE INFO

Keywords:
Selective Laser Melting
High Cycle Fatigue
Low Cycle Fatigue
Stainless steel
Aluminum alloy

ABSTRACT

In the last years, additive manufacturing has widely adopted to enable lightweight design based on the topological optimization. In fact, this technology allows generation of lattice structures with complex geometries and small thicknesses. In this work, both the low-cycle-fatigue and high-cycle-fatigue behaviors of selective laser melted AISI 316L and AlSi10Mg were investigated. Fatigue samples were designed to characterize small parts and tested in the as-built condition since reticular structures are usually adopted without any finishing operation. Microstructural features were studied by light-optical microscopy and scanning-electron microscopy. Finally, fatigue failures were studied considering the fracture mechanics principles with the Kitagawa-Takahashi diagram. The analysis of fracture surfaces revealed that crack nucleation mainly occurs close to the surface because of both poor surface quality and presence of near-surface defects. As expected, because of the face-centered cubic lattice, the final rupture of all the investigated alloys was characterized by micro-dimples confirming the presence of a ductile behavior.

1. Introduction

Additive manufacturing was established in the last decade and nowadays its use is still growing. A lot of alloys are available on the market, but their metallurgical and mechanical properties can change significantly according to the machine and process parameters, the building strategy and orientation and the powder size and morphology. In the as-built condition, AM components are characterized by textured tracks related to the scanning strategy [1]. Because of the high cooling rates, the microstructure shows very fine columnar dendrites and cell structures whose morphology and size strongly depend on the process parameters. Further modifications can be related to partial re-melting induced by layers deposition [2,3]. The high cooling rates are also responsible for a great difference between the inter-dendritic microstructure and chemical composition and the center-dendrite ones [4]. One of the most critical drawbacks of this technology is related to the residual porosity that almost always affect the produced parts. Such defects are mainly concentrated in the regions close to the outer surface rather than in the inner regions. Moreover, the poor surface roughness combined with the sub-surface porosity can decrease mechanical properties, in particular the fatigue resistance, significantly.

This project aims at investigating the static and dynamic properties of two AM alloys, AISI 316L and AlSi10Mg. In particular, after the metallurgical characterization by metallography, hardness, microhardness and tensile tests, the high-cycle- (HCF) and the low-cycle-fatigue (LCF) behavior was studied by axial fatigue tests. The analysis of the fracture surfaces by scanning electron microscope (SEM) revealed the fatigue micro-mechanisms.

AISI 316L is an austenitic chromium-nickel stainless steel, which combines good ductility with high corrosion resistance. It is adopted in several engineering applications, such as automotive, oil and gas, construction, chemical and petrochemical industries [5,6]. The good mechanical strength in the as-built AM condition is determined by presence of refined microstructures and high dislocation densities [6–8]. Regarding fatigue performances, some authors [9–11] found a lower fatigue limit in the as-built AM condition with respect to the conventionally-manufactured material [12]. The authors attributed such loss to presence of defects and poor surface finishing in the as-built AM condition.

The second material is an AlSi10Mg aluminum alloy. Al-Zn-Mg-Cu and Al-Cu-Mg-Si alloys offer large opportunities to achieve high mechanical performances after age hardening. However, regarding the AM technique, their processability is limited by hot-cracking phenomena

* Corresponding author.
E-mail address: davide.panzeri@polimi.it (D. Panzeri).

https://doi.org/10.1016/j.ijfatigue.2023.107931
Received 27 July 2023; Received in revised form 31 August 2023; Accepted 4 September 2023
Available online 9 September 2023

Nomenclature

Acronyms

AM	Additive Manufacturing
FCC	Face-Centered Cubic
BCC	Body-Centered Cubic
SLM	Selective Laser Melting
BCT	Body-Centered Tetragonal
TCP	Topologically Close Packed
UTS	Ultimate Tensile Strength
YS	Yield Strength
LOM	Light Optical Microscope
SEM	Scanning Electron Microscope
K-T	Kitagawa-Takahashi
QS	Quasi Static
HCF	High Cycle Fatigue
LCF	Low Cycle Fatigue
EDS	Energy-Dispersive Spectroscopy
PM	Permanent Mold
HPVD	High-Pressure Vacuum Die
R-O	Ramberg-Osgood
BCM	Basquin-Coffin-Manson

Symbols

β'	phase in aluminum alloys
β''	phase in aluminum alloys
R	fatigue load ratio
P	defect perimeter
A	defect area
R_a	surface roughness parameter
R_t	surface roughness parameter
R_z	surface roughness parameter
R_c	surface roughness parameter
R_v	surface roughness parameter
d	defect size
e	surface distance of the defect
HV	Vickers Hardness
ΔF	force increment
$\Delta\sigma$	stress interval
Δa	crack extension
F_i	stair-case force level
k	Dixon factor
x_F	stress level of the last stair-case test
K	Stress Intensity Factor
$\sqrt{area}$	defect size parameter (equivalent micro-notch length)
t	defect depth
ΔK_{th}	threshold stress-intensity range
$\Delta\sigma_f$	fatigue limit
α	constant
σ	applied stress
Y	constant
a_0	intrinsic El-Haddad crack length
$\Delta K_{th,LC}$	threshold ΔK for long cracks
$\Delta K_{th,eff}$	intrinsic (effective) ΔK threshold
h	Burgers vector component
k	Burgers vector component
l	Burgers vector component
E	elastic modulus
$\boldsymbol{b}$	Burgers vector
a	edge length of the unit cell
$\Delta\sigma_{th}$	threshold fatigue stress range
a_o'	modified a_0 parameter
a^*	additional parameter
ρ	density
σ_f	fatigue limit (50 % failure probability)
a	crack length
σ_{f0}	theoretical fatigue limit
ε_a	total strain amplitude
ε_{ae}	elastic portion of the total strain amplitude
ε_{ap}	plastic portion of the total strain amplitude
σ_a	stress amplitude
K	material constant
n	material constant
N_f	number of cycles at failure
ε_f'	fatigue ductility coefficient
σ_f'	fatigue strength coefficient
$2N_f$	number of reversals to failure
b	fatigue strength exponent
c	fatigue ductility exponent

Table 1
Chemical composition (wt. %) of the powders adopted in this work.

	Cr	Ni	Mo	Mn	Si	N	O
AISI 316L	17.9	13.9	2.81	1.56	0.29	0.08	0.04
	Si	**Mg**	**Fe**	**Ti**	**Mn**	**Cu**	**Ni**
AlSi10Mg	9–11	0.2–0.4	<0.55	<0.15	<0.45	<0.03	<0.04

occurring because of really high cooling rates in such innovative manufacturing technique [13,14]. Al-Si-Mg alloys, instead, have better castability and good response to aging treatment. Inside this class of materials, AlSi10Mg is one of the most employed for lightweight AM structures. In fact, its solidification behavior is well known and its mechanical properties are adequate in both the as-built and the age hardened conditions [14,15]. Solubilization and aging (T6-like treatment) were deeply investigated in the technical literature [16–19]. It was found that standard solution annealing, followed by fast quenching and artificial aging, transforms the fine α-Al cells and the Si segregation network into coarser grains and globular Si particles. Evidence of the laser tracks and the related heat-affected zones also disappeared during solubilization [16,18,20]. After solution treatment and aging, the percentage elongation significantly improves, but hardness, yield strength and ultimate tensile strength decrease significantly with respect to the as-built material. Tang et al. [21] and Beretta et al. [22] reported a large variability in the AlSi10Mg mechanical properties depending on sample orientation, process parameters and heat-treating conditions. The aging response of AlSi7Mg, an alloy similar to AlSi10Mg, was studied by Vedani et al., Yang et al. and Shi et al. using differential scanning calorimetry and micro-hardness tests [19,20,23]. They demonstrated that SLM-processed samples show the same precipitation sequence of the conventionally-cast material with formation of Mg-Mg, Si-Si and Mg-Si clusters, β'', β' and Mg_2Si phases together with Si precipitation.

2. Materials and methods

AISI 316L powder was supplied by LGC (Product IARM-FE316LP-18), whereas AlSi10Mg powder was produced by Sandvik (Product Osprey AlSi10Mg). The chemical composition of each AM powder is reported in Table 1. The specimens adopted in this experimental work were produced with process parameters optimized by the supplier and delivered in the as-built condition. The build direction corresponds to

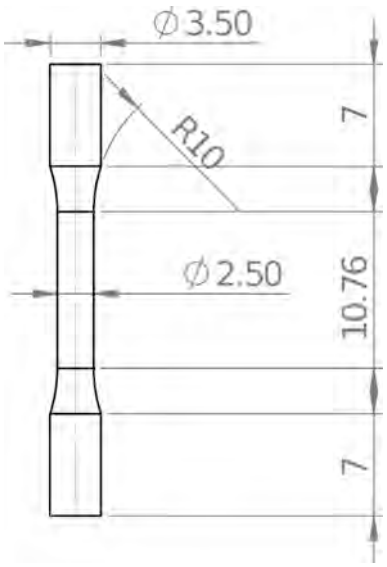

Fig. 1. Drawing of HCF and QS specimens adopted in this research work.

the longitudinal axis of each specimen, while the scanning plane lies on the transversal plane. Regarding AlSi10Mg, the powder particles have a spherical morphology with size from 20 μm to 63 μm. For AISI 316L, a spherical powder was adopted with size ranging between 11 μm and 88 μm.

The mechanical performance of AM parts depends on several factors strongly related to the printing technique. In particular, the microstructural features and the defects amount, distribution and morphology have a huge influence on both the fatigue resistance and the fracture toughness. Moreover, the surface finishing has an outstanding effect on fatigue crack initiation. For these reasons, the authors planned a wide characterization of the considered alloys for quality assessment purposes and to compare a fatigue prediction tool, such as the Kitagawa-Takahashi diagram, with the experimental results.

2.1. Determination of the surface roughness

Since surface roughness has a great influence on fatigue crack nucleation, it was measured using a Taylor-Hobson contact profilometer. Different roughness parameters (R_a,R_t,R_z,R_v,R_c) were measured according to EN ISO 21920-2:2022 standard [24] to characterize the surface in the as-built condition.

2.2. Metallographic analysis

From the vertically-printed specimens, metallographic sections were taken on planes parallel (longitudinal section) and perpendicular (transversal section) to the build direction. They were prepared according to the conventional metallographic procedure and observed by light optical (LOM) and scanning electron (SEM) microscopes after etching. Mounting of specimens was performed using cold-setting resin. Using an image analysis software, the porosity fraction and the area, roundness and distribution of defects were determined for each material. The roundness parameter was defined considering Equation (1).

$$\text{Roundness} = \frac{P^2}{4\pi A} \tag{1}$$

where A and P are the defect area and perimeter, respectively.

Since such defects are detrimental to the fatigue resistance, they were classified into different classes, i. e. surface single, surface clusters, inner single and inner cluster defects. In the considered materials, most of the pores concentrate in sub-surface regions. So, it is possible to define three possible crack nucleation promoters: surface roughness, near-surface single and cluster pores, and inner single and cluster pores. About near-surface defects, the Murakami's theory [25] points out the difference among shallow or deep flaws and all the others. The surface roughness can be converted into an equivalent micro-notch following the Murakami's approach [25]. Being the roughness continuously distributed on the whole surface circumference, it was considered as a shallow defect with depth equal to the R_v parameter [22].

2.3. Determination of the static mechanical properties: hardness, micro-hardness and tensile tests

Selective Laser Melting is a production technique really different from the conventional ones. For this reason, the mechanical properties (elastic modulus, yield strength, ultimate tensile strength and hardness) must be determined carefully. Hardness tests (HV2) were carried out on both transversal and longitudinal sections of all the considered materials to study possible anisotropic behavior. Moreover, micro-hardness profiles were performed from the outer surfaces till the specimen center to detect possible hardness variations able to influence the fatigue limit. Then, the room temperature tensile properties were determined by Quasi-Static (QS) tensile tests with crosshead speed equal to 0.1 mm/min. The tensile specimen geometry is equal to that adopted for HCF tests, as shown in Fig. 1.

2.4. High-cycle-fatigue (HCF) tests

HCF tests with load ratio R = 0 were performed using a STEPLab-UD04 machine (maximum load 5 kN and maximum frequency 35 Hz), according to ASTM E466 standard [26–28]. The drawing of the cylindrical specimens is reported in Fig. 1. The choice of a load ratio $R = 0$ is very common in the technical literature for axial fatigue tests. Nevertheless, when the service application involves other loading conditions and stress ratios, tests should be planned to reproduce as much as possible the real situation. In fact, the technical literature [29–31] shows that both the load ratio R and the mean stress influence the fatigue resistance significantly. Similarly, the frequency of load application can affect the results, especially in the high or very high regime. In particular, the combination of test frequency and applied fatigue stress is important because the specimen temperature can increase a lot. Nevertheless, when the very-high-cycle fatigue behavior is investigated, higher frequencies are necessary to reduce the test time. In these cases, the experimental set-up must be properly designed to prevent or minimize undesired effects, such as specimens overheating, as described in [29–31]. Considering the limited number of samples, the short staircase statistical approach was adopted to determine the fatigue limits [32–34]. Tests were conducted considering different load levels considering a stress increment equal to 10 MPa (force increment equal to 50 N).

A first test is conducted at the starting force level, F_1. This value, which should be as close as possible to the fatigue limit, is estimated from literature for each tested material. If the specimen withstands the run-out condition, 5×10^6 cycles, a subsequent test is performed at a force level increased by the force increment, i. e. $F_{i+1} = F_i + \Delta F$. Conversely, if the test ends with a failure, the following one is conducted at a force decreased by the force increment, i. e. $F_{i+1} = F_i - \Delta F$. Five tests for each material were performed. In addition to the number of failures (X) and run-outs (O), their order is considered to determine the fatigue limit in each material. The short stair-case method [35] determines the fatigue limit through a coefficient k, called Dixon factor and tabulated in [35]. Its value depends on the sequence of failures and run-outs. Equation (2) describes the calculation of the fatigue limit and x_F is the stress level of the last test.

$$\sigma_f = x_F + k\Delta\sigma \tag{2}$$

As said previously, surface roughness and sub-surface defects can

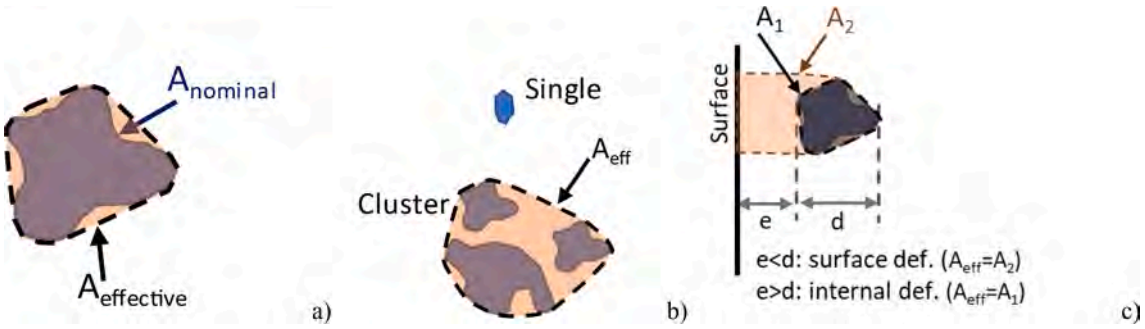

Fig. 2. Definition of the convex effective area of single defects (a) and cluster of defects (b) with and without presence of defect-surface interaction (c). Classification and analysis according to the Murakami's method [25].

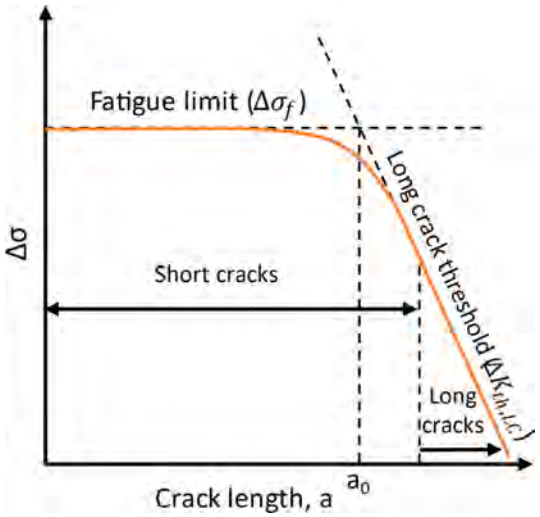

Fig. 3. Kitagawa-Takahashi diagram.

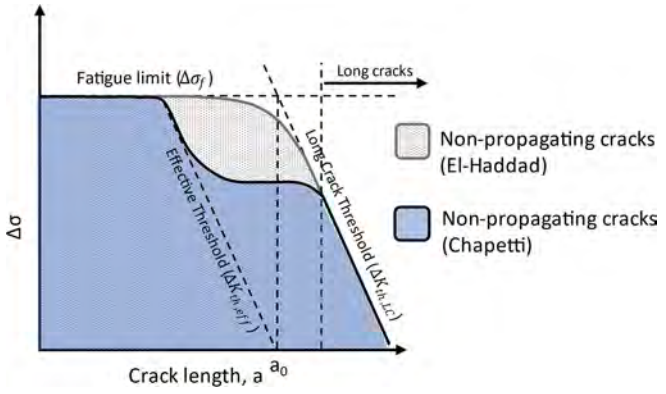

Fig. 4. Comparison between the approaches of El-Haddad and Chapetti.

affect the fatigue resistance greatly. Assuming such defects as a single equivalent flaw, fracture mechanics principles allows a deeper understanding of the fatigue life. Given the applied nominal stress σ, the Murakami's approach [25] suggests Equation (3) to relate each defect to the applied stress-intensity factor K.

$$K = \sigma Y \sqrt{\pi \sqrt{area}} \tag{3}$$

Y is equal to 0.65 and 0.50 for surface and internal defects, respectively. Regarding Equation (3), the difference between the Y values suggests that surface defects are more critical than inner ones. So, given a certain stress, in order to obtain the same K value, the size parameter $\sqrt{area}$ of an inner flaw must be 1.69 times higher than that of a surface defect. $\sqrt{area}$ is the effective length of the equivalent micro-notch calculated from the convex area of the defect determined according to the Murakami's method [25], as shown in Fig. 2.a. This parameter is very important since it is related to the shape, dimension and position of each defect. If only a single defect is present, the area is calculated as the convex contour which envelopes the original irregular shape, as shown in Fig. 2.a. When multiple defects are present, interaction among them must be considered. A cluster is obtained when distances between adjacent defects are lower than the equivalent diameter of the smallest defect within the cluster, as shown in Fig. 2.b. The cluster is characterized considering the convex area which circumscribes all the defects belonging to the cluster. Then, the Murakami's approach considers the interaction of sub-surface defects with the surface [25]. Referring to Fig. 2.c, when the distance from the surface, e, is higher than the defect size, d, the defect-surface interaction is negligible. Other authors [36] suggested to consider the $\sqrt{area}$ parameter instead of the defect size to assess the presence of defect-surface interaction.

Regarding surface shallow defects, such as the surface roughness and surface defects with length-to-width ratio higher than 10, the effective length of the equivalent flaw is no longer calculated through the $\sqrt{area}$ size parameter, but considering the defect depth, t, as described by the Murakami's method [25]. So, in this case, calculation of the stress-intensity factor is performed considering Equations (4) and (5).

$$K = \sigma Y \sqrt{\pi \sqrt{area_{shallow}}} \tag{4}$$

$$\sqrt{area_{shallow}} = \sqrt{10}t \tag{5}$$

The correct and precise identification of the defect type (surface, sub-surface, inner and shallow) is one of the most important aspects for estimating the fatigue resistance on the base of the existing defects that can be identified by destructive (metallographic analysis) or non-destructive (X-ray tomography) tests. Such analysis is fundamental to accurately determine the K value of each defect and consequently also the fatigue behavior. For instance, Fig. 2 remarks that pores forming clusters behave like a larger defect with an equivalent size which is higher than that of the largest pore of the cluster. Moreover, the classification of a flaw as a surface defect involves an applied stress intensity factor which is 30 % ($Y_{surface}/Y_{inner} = 1.3$) higher compared to that of an inner pore with the same size parameter. The stress-intensity factor K is very useful to study the fatigue behavior. Particularly, El-Haddad et al. [37] suggested a relation between the threshold ΔK (ΔK_{th}) and the fatigue limit ($\Delta\sigma_f$) defining an intrinsic crack, a_0, that considers the overall effect of existing defects, microstructure, non-metallic inclusions, micro-damages induced by the manufacturing process. The relation among fatigue stress, threshold ΔK and crack length is summarized by the Kitagawa-Takahashi diagram [38] shown in Fig. 3.

Equation (6) defines the intrinsic El-Haddad crack.

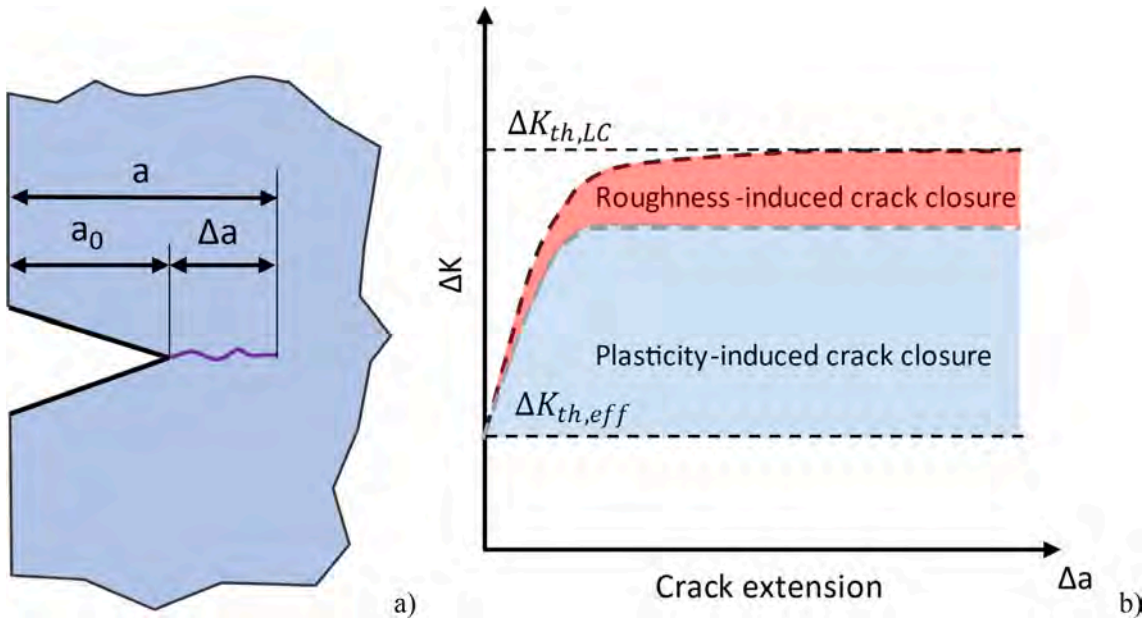

Fig. 5. Definition of the crack length, the initial crack and the crack extension (a); R-curve between the stress intensity range and the crack extension (b).

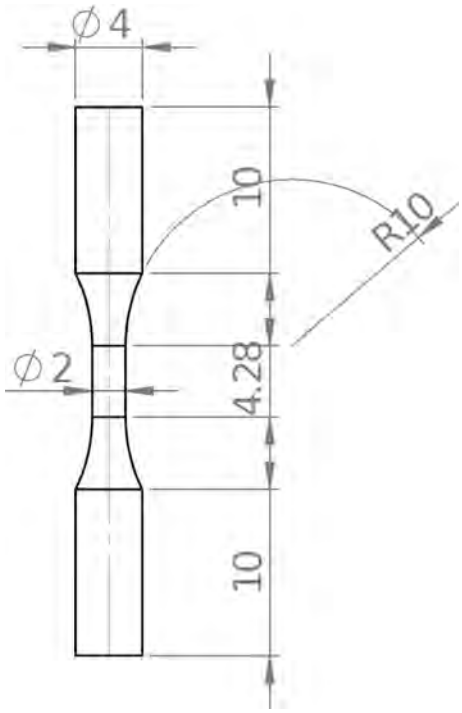

Fig. 6. Drawing of LCF specimens adopted in this work.

$$a_o = \frac{1}{\pi}\left(\frac{\Delta K_{th,LC}}{Y\Delta\sigma_f}\right)^2 \tag{6}$$

where $\Delta K_{th,LC}$ is the threshold ΔK for long cracks and $\Delta\sigma_f$ represents the fatigue limit.

However, when a crack is not associated to complete crack closure build-up, such as short cracks, the threshold ΔK is reduced with respect to that of long cracks [39,40]. Consequently, compared to the Chapetti's approach [41], the El-Haddad model is non-conservative, as shown in Fig. 4. Different methods were proposed to describe the crack closure build-up through exponential functions or other models which tend to the long cracks ΔK_{th} threshold asymptotically [41–43]. As a result, the R-curve shown in Fig. 5 relates the threshold stress intensity range to the crack extension. Furthermore, investigating the effects of pre-existing

Table 3
Surface roughness, inner and surface defects observed in AISI 316L specimens.

Roughness Max R_v [μm]	Micro-notch length Roughness [μm]	Surface single and cluster defects [μm]	Inner single and cluster defects [μm]
37.4	118	142 (max.)	82 (max.)

Table 4
Surface roughness, inner and surface defects observed in AlSi10Mg specimens.

Roughness Max R_v [μm]	Micro-notch length Roughness [μm]	Surface single and cluster defects [μm]	Inner single and cluster defects [μm]
18.7	59	226 (max.)	187 (max.)

Table 2
Roughness parameters measured on the investigated materials.

AISI 316L	Min [μm]	Max [μm]	Average [μm]	AlSi10Mg	Min [μm]	Max [μm]	Average [μm]
R_a	6.3	12.7	9.2	R_a	4.5	10.4	7.2
R_t	46.7	73.3	62.0	R_t	39.3	53.5	47.4
R_z	43.2	71.1	58.9	R_z	35.3	46.1	41.1
R_c	21.0	45.6	31.5	R_c	14.5	27.5	21.4
R_v	19.8	37.4	28.9	R_v	15.0	18.7	17.2

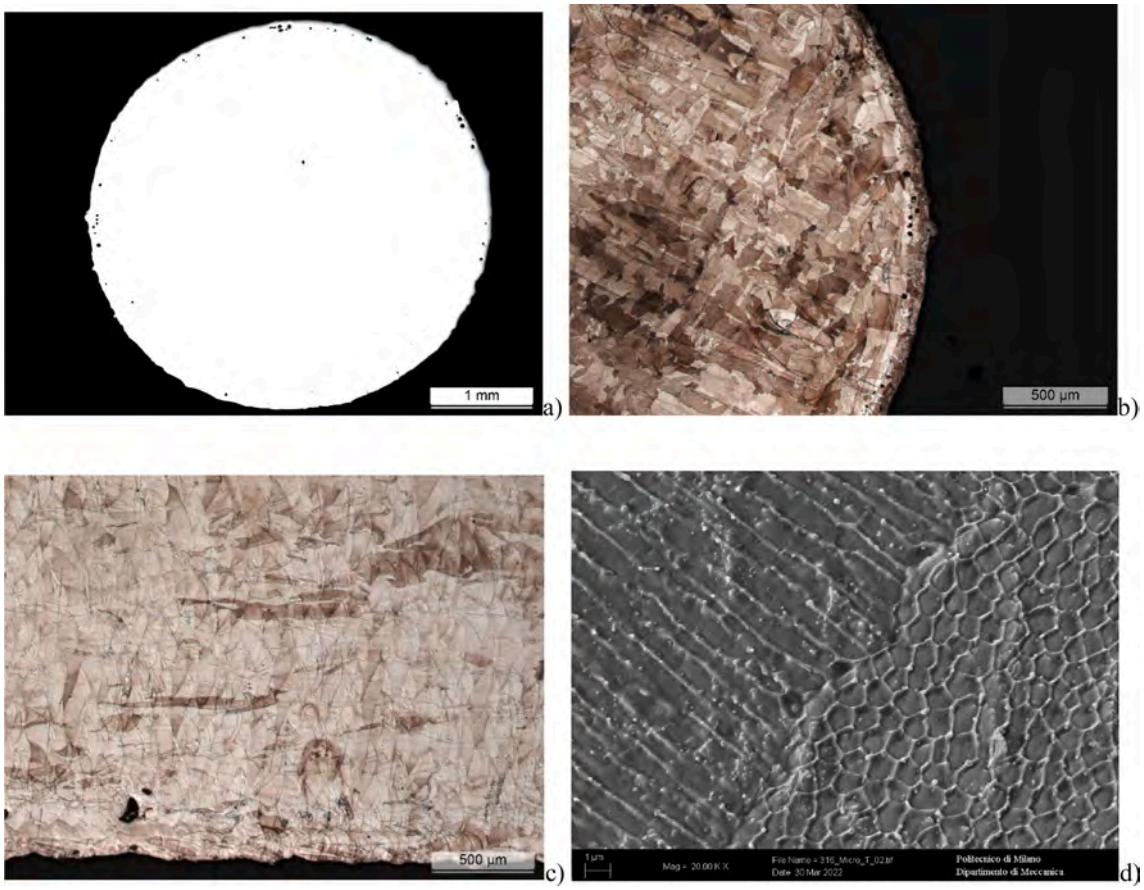

Fig. 7. Microstructure observed in the transversal (a, b) and longitudinal directions (c). SEM image in the transversal plane (d).

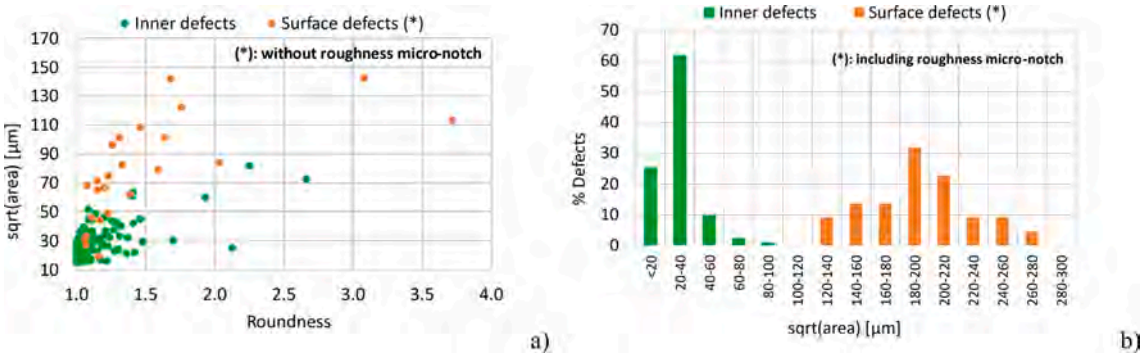

Fig. 8. Analysis of the observed defects. (a) Relation between roundness and micro-notch length; (b) Distribution of inner and surface porosity.

flaws considered as sharp notches, Tanaka and Akiniwa [39] found that the region of non-propagating cracks gets smaller when the defect length increases.

The intrinsic (effective) threshold, $\Delta K_{th,eff}$, does not depend neither on the microstructure nor the load ratio, but only on material physical properties. The scientific literature proposes different relations to determine its value. Li et al. [44] reported some models mainly based on the elastic modulus, as shown in Equation (7).

$$\Delta K_{th,eff} = \alpha\sqrt{|\boldsymbol{b}|}E \tag{7}$$

where E is the elastic modulus, $\boldsymbol{b}$ is the Burgers vector and α is equal to 0.75 according to Pippan et al. [45]. The Burgers vector, defined by Equation (8), is a function of the lattice parameters.

$$|\boldsymbol{b}| = \frac{a}{2}\sqrt{h^2 + k^2 + l^2} \tag{8}$$

where a is the edge length of the unit cell, while h, k and l are the Burgers vector components. In the FCC lattice, the directions $\langle 1,1,0\rangle$ are the most prone to slide. For such directions, the Burgers vector is equal to $|\boldsymbol{b}| = \frac{a}{2}\sqrt{2}$.

To consider the ΔK_{th} variation described by the R-curve, some authors [41,46] suggested an expression slightly different from the El-Haddad one shown in Equation (9). This relation is reported in Equation (10).

$$\Delta\sigma_{th} = \frac{\Delta K_{th,LC}}{Y\sqrt{\pi(a + a_o)}} \tag{9}$$

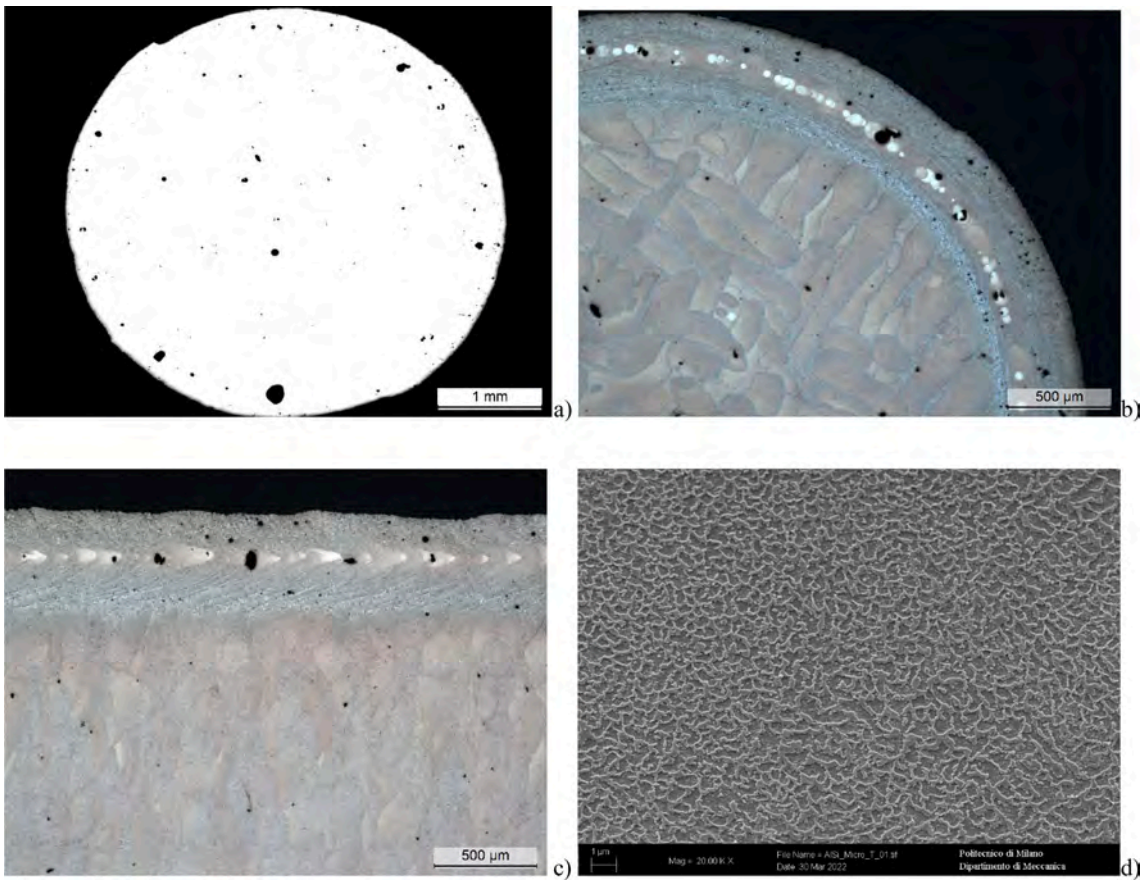

Fig. 9. Microstructure observed in the transversal (a, b) and longitudinal directions (c). SEM image in the transversal plane (d).

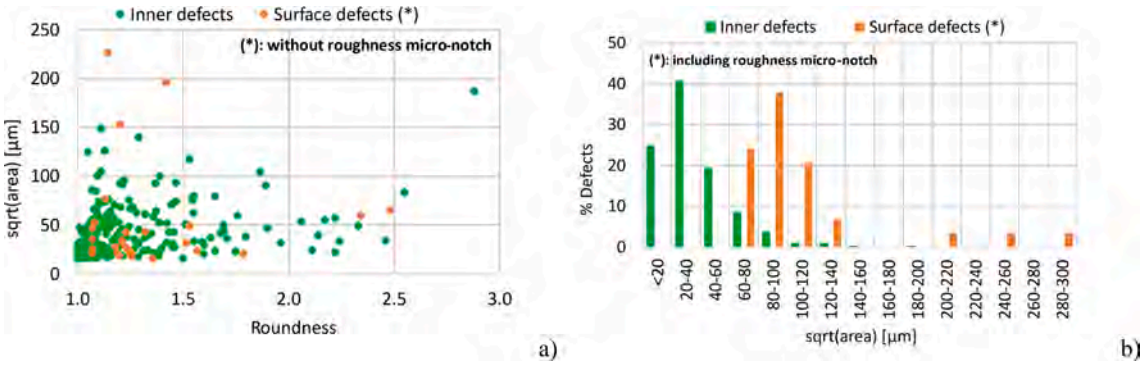

Fig. 10. Analysis of the observed defects. (a) Relation between roundness and micro-notch length; (b) Distribution of inner and surface porosity.

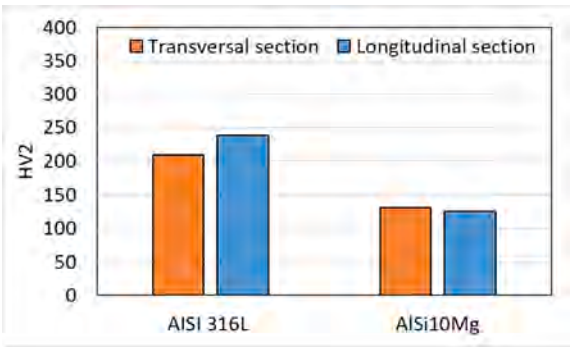

Fig. 11. Hardness values of the investigated alloys.

$$\Delta\sigma_{th} = \frac{\Delta K_{th}(a)}{Y\sqrt{\pi(a+a_o)}} \tag{10}$$

The limit curve based on the intrinsic (effective) $\Delta K_{th,eff}$ results in the non-propagating Chapetti region shown in Fig. 4. Replacing the El-Haddad parameter a_0 with the modified value $a_0^{'}$ (Equation (11), a new limit stress curve is obtained as shown in Equation (12).

$$a_o^{'} = \frac{1}{\pi}\left(\frac{\Delta K_{th}(a)}{Y\Delta\sigma_f}\right)^2 \tag{11}$$

$$\Delta\sigma_{th} = \frac{\Delta K_{th}(a)}{Y\sqrt{\pi(a+a_o^{'})}} \tag{12}$$

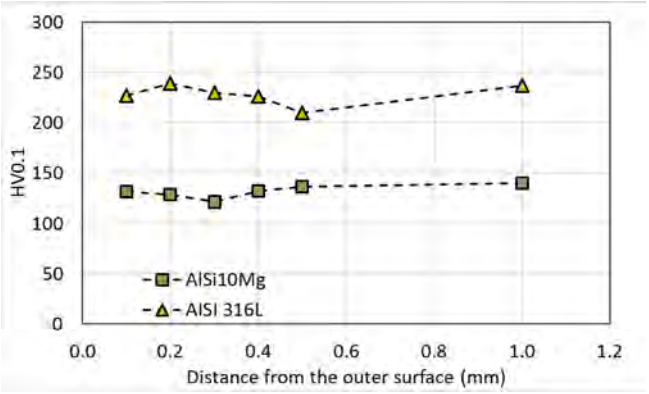

Fig. 12. Micro-hardness profiles varying the distance from the outer surface.

Table 5
Tensile properties of the investigated materials.

Material	YS [MPa]	UTS [MPa]	E [GPa]
AISI 316L	465	540	180
AlSi10Mg	233	352	70

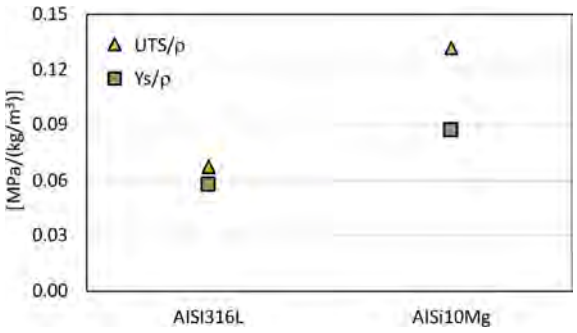

Fig. 13. Comparison among the specific strengths of the investigated materials.

2.5. Low-cycle-fatigue (LCF) tests

Low-cycle-fatigue (LCF) fully-reversed tensile-compression tests were performed on cylindrical specimens (Fig. 6) according to the standard ASTM E606 [47]. Because of the small specimen size, the LCF tests were performed in displacement control. The strain was calculated adjusting the imposed displacement with that related to the testing machine stiffness. The latter was determined experimentally before the LCF tests. Finally, the strain was obtained dividing such corrected displacement by the specimen cylindrical length. Because of the limited number of specimens, four samples per material were tested.

The test frequency was set equal to the minimum value prescribed by the standard, i.e. 0.1 Hz [48]. This value was selected to prevent possible samples overheating that could affect the results.

Table 6
Fatigue limits of the investigated alloys.

Material	σ_f [MPa]	$\frac{\sigma_f}{UTS}$
AISI 316L	136	0.25
AlSi10Mg	123	0.35

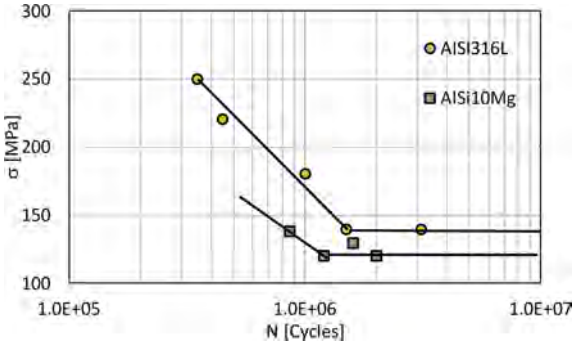

Fig. 15. Wöhler diagram for the tested alloys.

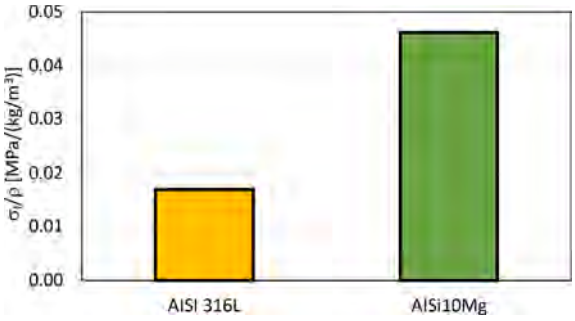

Fig. 16. Comparison among specific fatigue limits.

2.6. Determination of the fatigue micro-mechanisms

The investigation of the influence of surface and the inner defects on fatigue crack nucleation and propagation requires a deep observation of the microscopic aspects of fracture surfaces. For such a reason, selected broken fatigue specimens of both HCF and LCF tests were investigated by SEM at different magnifications highlighting the nucleation and propagation zones as well as the killer defect/s.

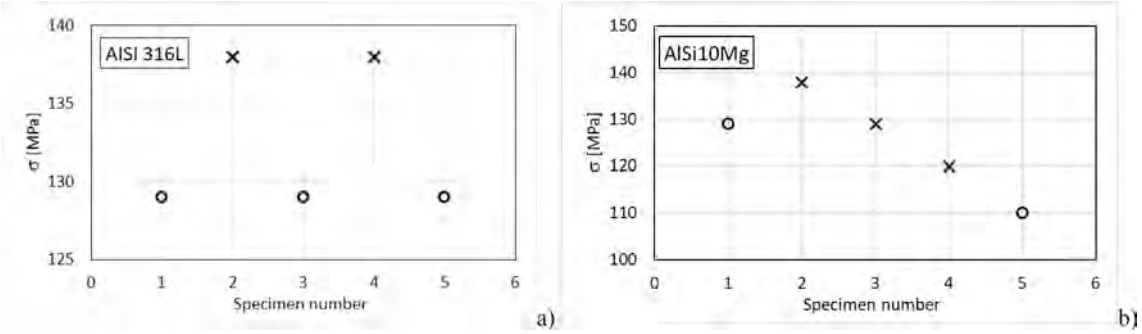

Fig. 14. Testing sequences for the investigated alloys.

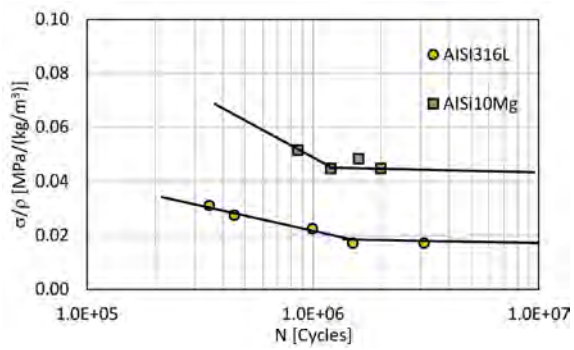

Fig. 17. Comparison among the specific-strength-modified Wöhler curves.

Table 7
Calculated $\Delta K_{th,eff}$ and $\Delta K_{th,LC}$ for the investigated materials.

Material	$\Delta K_{th,eff}$ [MPa$\sqrt{m}$]	$\Delta K_{th,LC}$ [MPa$\sqrt{m}$]
AISI 316L	2.1	5.7
AlSi10Mg	1.0	4.7

3. Surface roughness analysis and metallographic investigation

3.1. Surface roughness tests

Five measurements were carried out per each material. The obtained results, reported in Table 2, confirm the low surface quality.

3.2. Metallographic investigation

The metallographic observations revealed a large number of micro- and macro-porosities, especially close to the outer surface, in a zone with radial width of approximately 120 μm and 180 μm for the AISI 316L stainless steel and AlSi10Mg, respectively. The percentage porosity was evaluated by image analysis in the transversal section at 25X magnification. It resulted equal to 0.7 % for AlSi10Mg and 0.2 % for AISI 316L. Porosity formation generally has two origins. The first one is related to the absorption of surrounding gases and/or the evaporation of alloying elements, the other is associated to the lack-of-fusion phenomenon, which depends on the building strategy [49,50]. All the as-built specimens show an outer contour layer, where most of the pores are concentrated.

In the transversal plane, the chemical etching revealed elongated tracks of melt pools with different orientations because of the layer-stacking technique. In the longitudinal plane, stacking of melt pools in the build direction is evident and characterized by an almost uniform orientation. They have a half-cylindrical shape, which is related to the Gaussian distribution of laser energy [51–56]. Melt pools are composed by fine dendrites surrounded by coarser traces among adjacent pools. SEM analysis revealed that the microstructure is characterized by presence of both cellular-shaped structures and elongated dendrites, whose growth occurred in different directions due to the heat flux orientation [51–56].

The characterization of the microstructural features in both the transversal and longitudinal sections is particularly important since AM components can be subjected in service to multi-directional loading. In

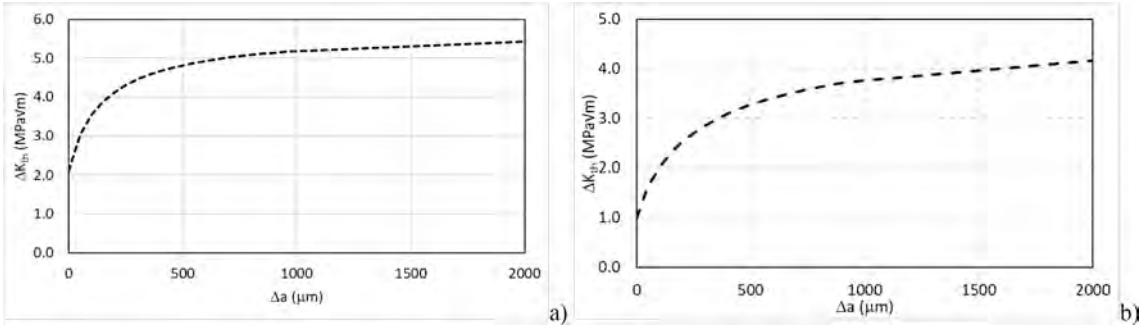

Fig. 18. Influence of crack length on the threshold ΔK. a) AISI 316L; b) AlSi10Mg.

Table 8
Calculated theoretical fatigue limits ($R = 0$) for surface (a) and inner (b) defects.

Material	HV2	$\sigma_{f0}(R = 0)$, Y = 0.65 [MPa] (a)	σ_{f0}/UTS	$\sigma_{f0}(R = 0)$, Y = 0.50 [MPa] (b)	σ_{f0}/UTS
AISI 316L	224	339	0.628	341	0.631
AlSi10Mg	129	172	0.489	172	0.489

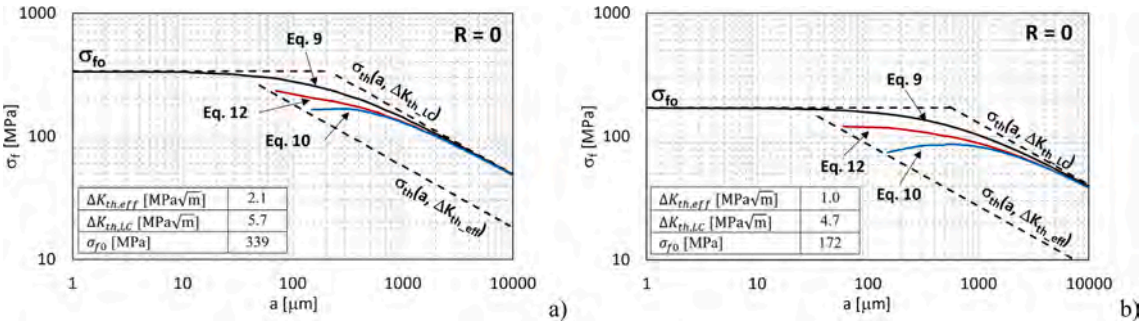

Fig. 19. Comparison among the limit curves for non-propagating cracks in the K-T diagram. a) AISI 316L; b) AlSi10Mg.

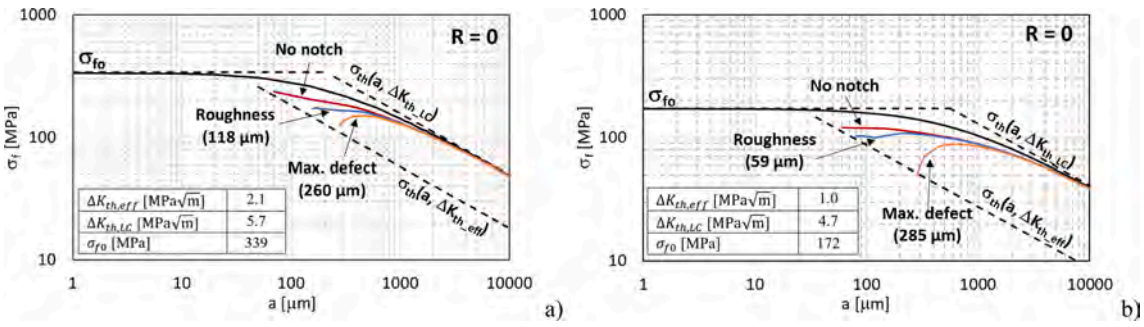

Fig. 20. Comparison among the limit curves varying the initial micro-notch length. a) AISI 316L; b) AlSi10Mg.

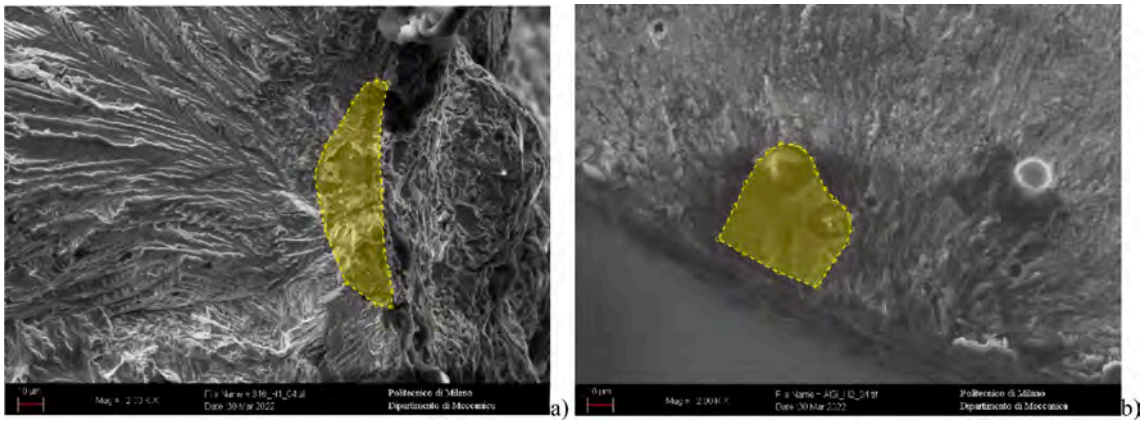

Fig. 21. Determination of the equivalent micro-notch length for surface and inner defects. (a) AISI 316L, (b) AlSi10Mg.

Table 9
Summary of nucleation sites, total micro-notch lengths and fatigue stresses related to broken fatigue specimens. (a) Conversion of the roughness parameter R_v into the equivalent micro-notch length; (b) conversion of the observed defect into an equivalent micro-notch; (c)=(a)+(b).

Material	Nucleation site	Surface Roughness R_v[µm]	Micro-notch (roughness) [µm] **(a)**	$\sqrt{area}$(defect) [µm] **(b)**	Micro-notch total length [µm] **(c)**	Fatigue stress [MPa]
AISI 316L	Surface porosity	37.4	118	41	159	249
	Surface porosity			57	175	215
	Surface porosity			79	197	138
	Surface porosity			121	239	138
AlSi10Mg	Surface	18.7	59	—	59	160
	Surface porosity			26	85	138
	Surface porosity			42	101	129

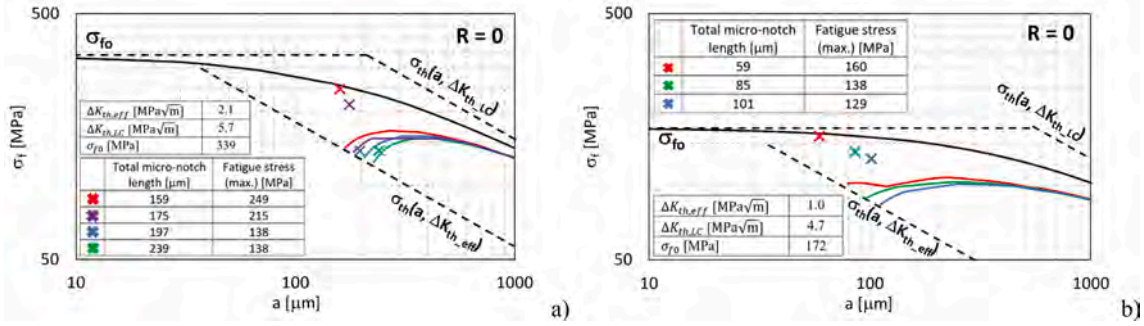

Fig. 22. K-T diagrams for the broken fatigue specimens summarized in Table 9. (a) AISI 316L; (b) AlSi10Mg.

the scientific literature [29–31], it is known that the static mechanical properties, the fatigue resistance, the fracture toughness and the long crack threshold $\Delta K_{th,LC}$ are deeply affected by the build direction and the powder size. For instance, Qian et al. [31] found a huge decrease of the fatigue limit when AM specimens are tested perpendicularly to the build direction. So, a careful microstructural investigation and a deep characterization of the defects size and morphology can give important information about the service performance of an AM part in the considered loading condition. For this reason, the authors performed a wide microscopic analysis focusing the attention on the microstructural

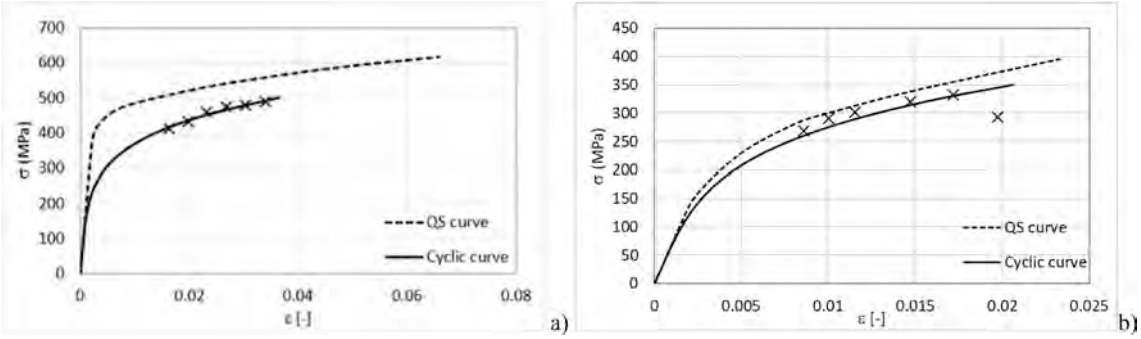

Fig. 23. Ramberg-Osgood cyclic curves compared to the quasi-static (QS) ones. (a) AISI 316L; (b) AlSi10Mg.

Table 10
Ramberg-Osgood parameters.

	K [MPa]	n [-]	E [GPa]
AISI 316L	1020	0.2102	180
AlSi10Mg	1005	0.2536	70

Table 11
Modified Basquin-Coffin-Manson parameters.

	σ_f' [MPa]	b [-]	ε_f' [-]	c [-]	$\varepsilon_{fatigue}$ [-]
AISI 316L	500	−0.30	0.30	−0.5	$4.40 \bullet 10^{-4}$
AlSi10Mg	300	−0.30	0.10	−0.4	$1.06 \bullet 10^{-3}$

features and the observed defects. They were classified into inner and surface flaws according to the Murakami's theory [25]. They are reported in Table 3 and Table 4 together with the surface roughness conversion into the equivalent micro-notch. Since crack nucleation is generally driven by the worst defect, the maximum R_v value was selected to represent the notch effect of the surface roughness [22]. The total length of each surface defect was obtained adding the length of the equivalent micro-notch to the roughness equivalent micro-notch.

3.2.1. AISI 316L stainless steel

Melt pools are clearly visible in both transversal (Fig. 7.a and Fig. 7.b) and longitudinal directions (Fig. 7.c). In the transversal direction, the elongated tracks of melt pools have different orientations, while, in the longitudinal building direction, an almost uniform shape and orientation is observed. The presence of a contour layer is visible too. As shown in Fig. 7.d, a cellular-shaped structure combined with elongated dendrites is present, as described in the technical literature [57–60]. A large number of pores was observed as well, mainly concentrated in a subsurface region, as shown in Fig. 7.a.

The inner and surface defects are reported in Table 3.

Defects detected by metallographic analysis were converted into equivalent micro-notches and classified according to their roundness and distribution within the section, as shown in Fig. 8.

Table 12
Samples selected for SEM analysis of fracture surfaces and fatigue micro-mechanisms.

Material	Series	Code ID	Number of cycles to failure
AISI 316L	Low cycle fatigue	LCF1	250
AISI 316L	High cycle fatigue	HCF1	346,677
AISI 316L	High cycle fatigue	HCF2	1,640,950
AlSi10Mg	Low cycle fatigue	LCF1	13
AlSi10Mg	High cycle fatigue	HCF1	392,097
AlSi10Mg	High cycle fatigue	HCF2	853,349

3.2.2. AlSi10Mg alloy

Melt pools are clearly visible in both transversal (Fig. 9.a and Fig. 9.b) and longitudinal directions (Fig. 9.c). In the transversal direction, the elongated tracks of melt pools have different orientations, while, in the longitudinal building direction, they show an almost uniform shape and orientation. The melt pools within the surface contour layer show a clear V shape in the longitudinal building direction because of the different building parameters with respect to the inner zone. Moreover, SEM revealed a typical cellular-shaped structure made of a Si-rich network dispersed within the supersaturated aluminum matrix [51–53,56,57], as shown in Fig. 9.d. High number of pores are clearly visible in the whole section, especially in the surface contour zone.

The inner and surface defects are reported in Table 4.

Defects detected by metallographic analysis were converted into equivalent micro-notches and classified according to their roundness and distribution within the section, as shown in Fig. 10.

4. Hardness, micro-hardness and tensile tests

The hardness values of the investigated materials are compared in Fig. 11, whereas the micro-hardness profiles are reported in Fig. 12. No significant difference was found between the transversal and longitudinal sections of the AlSi10Mg alloy, whereas a slight hardness anisotropy was observed in AISI 316L. The micro-hardness profiles did not show any substantial difference between outer and inner zones.

Bartolomeu et al. [61] compared AISI 316L stainless steels produced

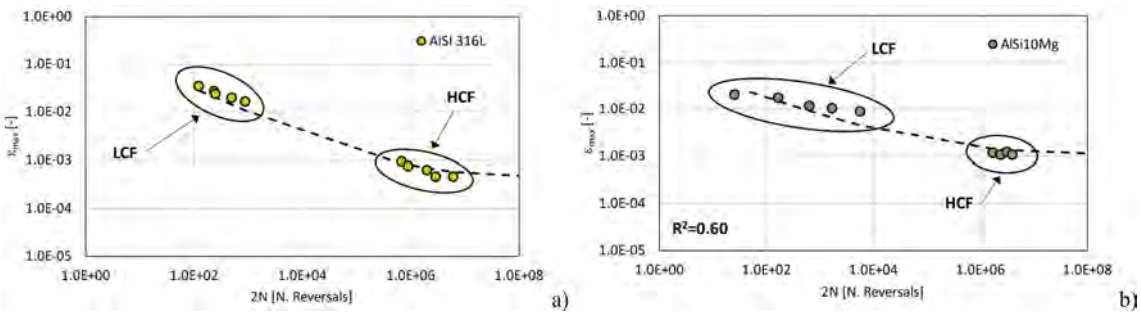

Fig. 24. Modified Basquin-Coffin-Manson curves for each investigated material.

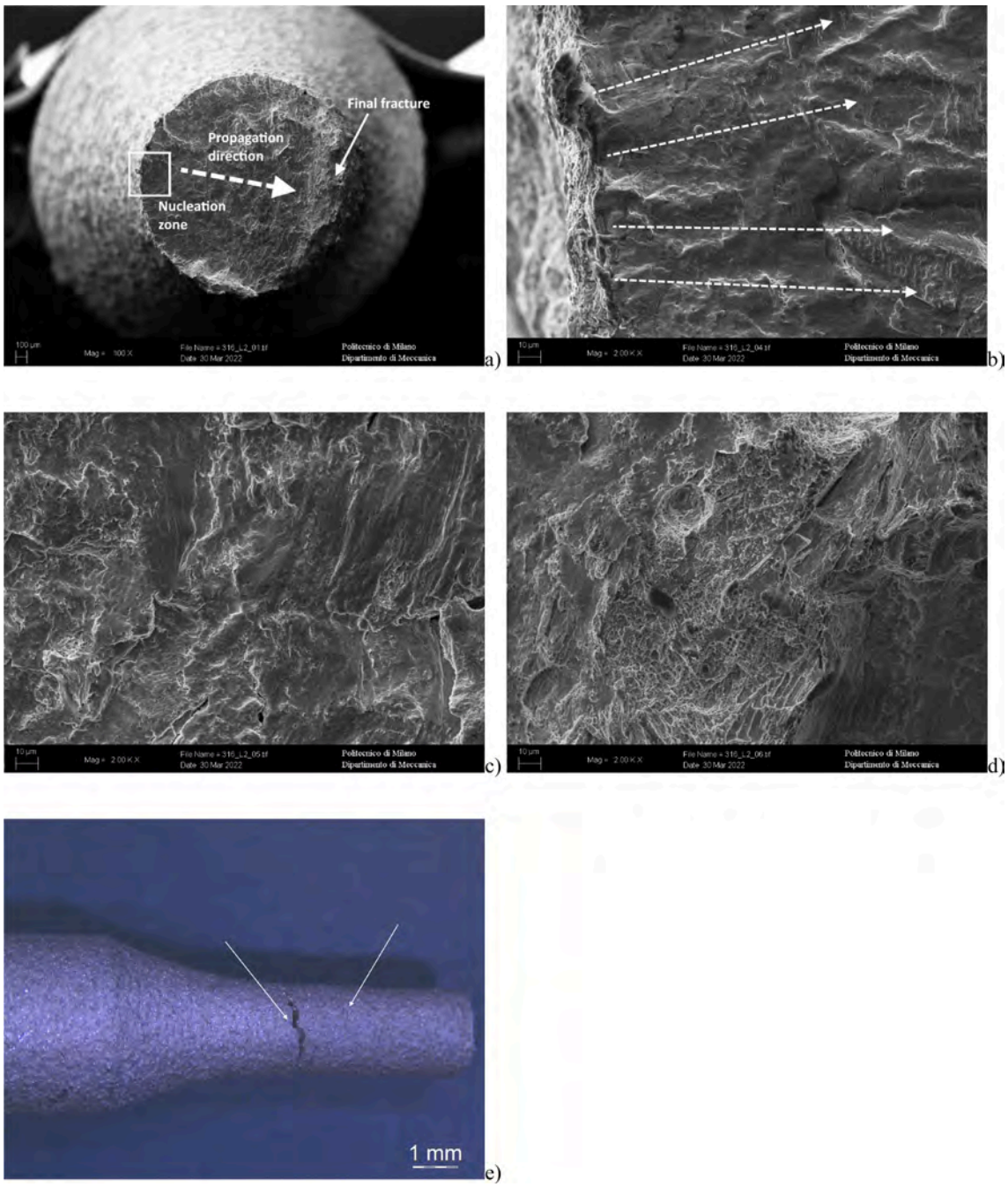

Fig. 25. Fracture surface analysis of specimen LCF1 - (a) fracture surface, (b) nucleation zone, (c) propagation zone, (d) final fracture. Multiple crack nucleation along the specimen gauge length, as shown in (e).

by different manufacturing techniques: conventional cast, hot pressing and selective laser melting. They found average hardness values from 150 HV to 230 HV. Liu et al. [62] investigated the mechanical properties of AlSi10Mg after permanent mold (PM) and high-pressure vacuum die (HPVD) casting in the T6 aging condition. They reported hardness values ranging from 110 HV to 120 HV. The previous data can be compared with those reported in Fig. 11 and Fig. 12. The average hardness of AISI 316L stainless steel is 224 HV and it is compatible with the literature data. Moreover, it is significantly higher than that of conventionally cast materials. For the AlSi10Mg alloy, the average hardness is equal to 129 HV, which is slightly higher than that reported by Liu et al. [62] for the T6 state.

The tensile properties are summarized in Table 5.

Except for the FCC lattice structure, the investigated materials are completely different. Particularly, density ρ [kg/m^3] represents a really important property in engineering applications. In the technical literature, the density of AISI 316L and AlSi10Mg are 8000 kg/m^3 and 2670 kg/m^3, respectively. The investigated alloys can be compared considering the specific strength, i.e. strength over density (YS/ρ and UTS/ρ). Fig. 13 shows that the aluminum alloy has the highest specific strength both in terms of UTS and YS.

5. High-cycle-fatigue (HCF) tests

For the AISI 316L stainless steel, the sequence of failures and run-outs is O-X-O-X-O, as shown in Fig. 14.a. The Dixon factor results equal to 0.701 leading to a fatigue limit of 136 MPa. For the AlSi10Mg alloy, the sequence of failures and run-outs is O-X-X-X-O, as reported in

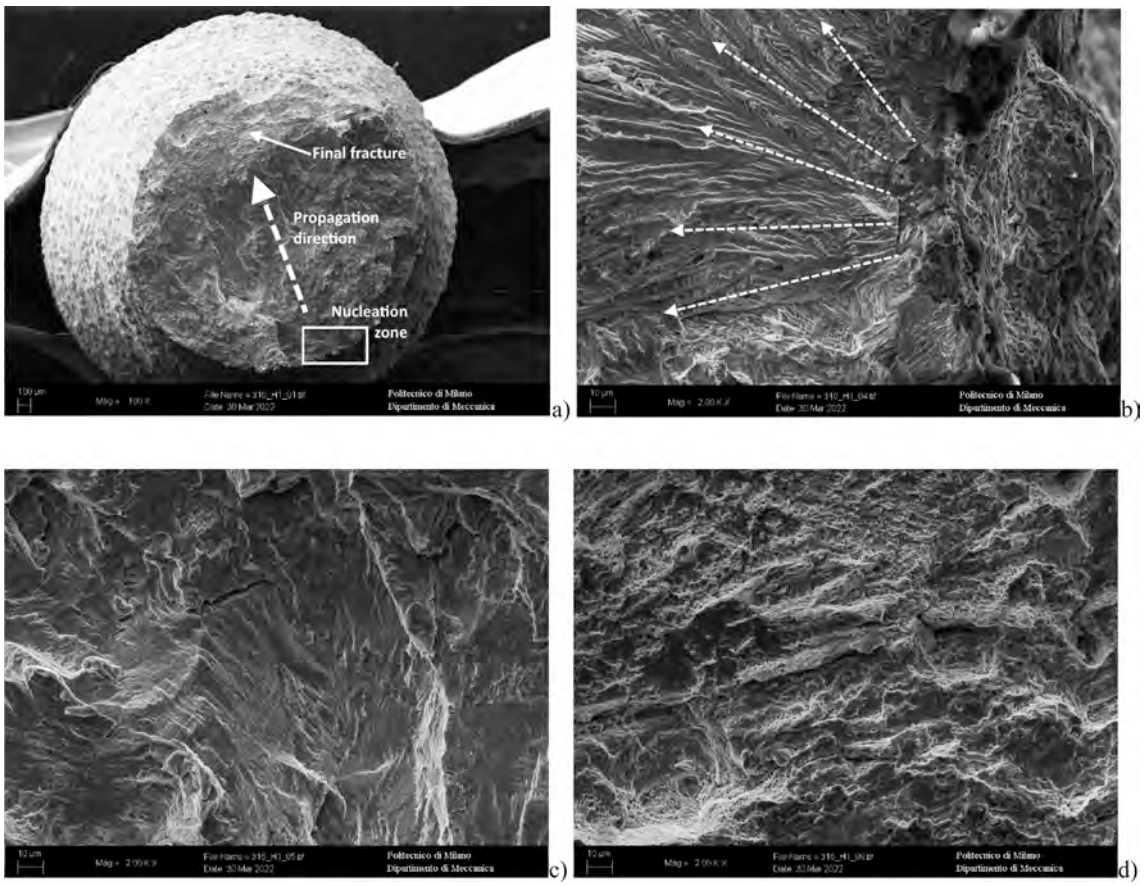

Fig. 26. Fracture surface analysis of specimen HCF1 - (a) fracture surface, (b) nucleation zone, (c) propagation zone, (d) final fracture.

Fig. 14.b. The Dixon factor is equal to 1.288 leading to a fatigue limit of 123 MPa. The fatigue limits, associated with 50 % failure probability, are summarized in Table 6.

In addition to the fatigue limit zone, tests were conducted in the finite life region. The resulting Wöhler curves are shown in Fig. 15.

Solberg et al. [9] studied the fatigue behavior of AM AISI 316L with load ratio $R = 0.1$, run-out condition equal to 2×10^6 cycles and surface roughness, R_a, equal to 10.1 μm. They found fatigue strength 20 % higher than that reported in Table 6. In the present paper, considering the similar surface roughness, the slightly lower load ratio and the higher run-out condition, the fatigue limit of 136 MPa can be considered comparable with that observed by Solberg et al. [9]. Moreover, considering the literature review reported by [63], the σ_f/UTS ratio for AM AISI 316L in the as-built condition is included between 0.26 and 0.40 with conversion to $R = 0$. Such range for the σ_f/UTS ratio is referred to an average number of run-out cycles equal to 1.7×10^6 with standard deviation of 0.6×10^6 [63]. Since the run-out condition adopted in this work was higher and equal to 5×10^6 cycles, the presence of a ratio close to the lower extremity of the literature range is hence justified.

Regarding AM AlSi10Mg, the σ_f/UTS ratio reported in Table 6 is compatible with the literature. In fact, as reported by [64], this ratio for AM AlSi10Mg in the as-built condition ranges from 0.18 to 0.49 when converted to $R = 0$.

Then, the investigated alloys were compared considering the ratio between fatigue limit and density. The specific fatigue limits are reported in Fig. 16, whereas the specific-strength-modified Wöhler curves are reported in Fig. 17.

As already observed in the comparison among the tensile properties, AlSi10Mg provides the best specific fatigue behavior confirming its importance in several engineering applications.

5.1. Kitagawa-Takahashi (K-T) diagram and limit curves

As discussed previously, the R-curve can be estimated considering different models at given $\Delta K_{th,eff}$ and $\Delta K_{th,LC}$ values. In this work, the authors adopted the model defined by Zerbst et al. [43] and reported in Equation (13).

$$\Delta K_{th} = \Delta K_{th,LC}\sqrt{\frac{\Delta a + a^*}{\Delta a + a^* + a_o}} \tag{13}$$

$\Delta K_{th,LC}$ is the threshold ΔK for long cracks, a_0 is the El-Haddad intrinsic crack and a^* is an additional parameter adopted to make $\Delta K_{th} = \Delta K_{th,eff}$ when $\Delta a = 0$. The a^* parameter is defined by Equation (14).

$$a^* = a_o\frac{\left(\Delta K_{th,eff}/\Delta K_{th,LC}\right)^2}{1 - \left(\Delta K_{th,eff}/\Delta K_{th,LC}\right)^2} \tag{14}$$

The intrinsic (effective) $\Delta K_{th,eff}$ threshold was determined for each material with Equation (7) considering the parameter α equal to 0.75 as suggested by Pippan [40,45,46,65]. The $\Delta K_{th,LC}$ threshold depends on microstructure and process parameters. It was determined after a wide literature review. About AISI 316L stainless steel, values included between 2.4 MPa$\sqrt{m}$ and 9.9 MPa$\sqrt{m}$ are reported [66–68]. For AlSi10Mg, some authors [22,64,69] reported threshold data included between 1.3 MPa$\sqrt{m}$ and 6.9 MPa$\sqrt{m}$. The adopted $\Delta K_{th,eff}$ and $\Delta K_{th,LC}$ values are finally summarized in Table 7. Then, the influence of crack length on the threshold ΔK is reported in Fig. 18.

The theoretical fatigue limit, σ_{f0}, is necessary to determine the K-T diagram. Such limit should be determined considering fatigue specimens with the same microstructural features of the investigated materials, but without surface and inner defects. For additively-manufactured parts, its

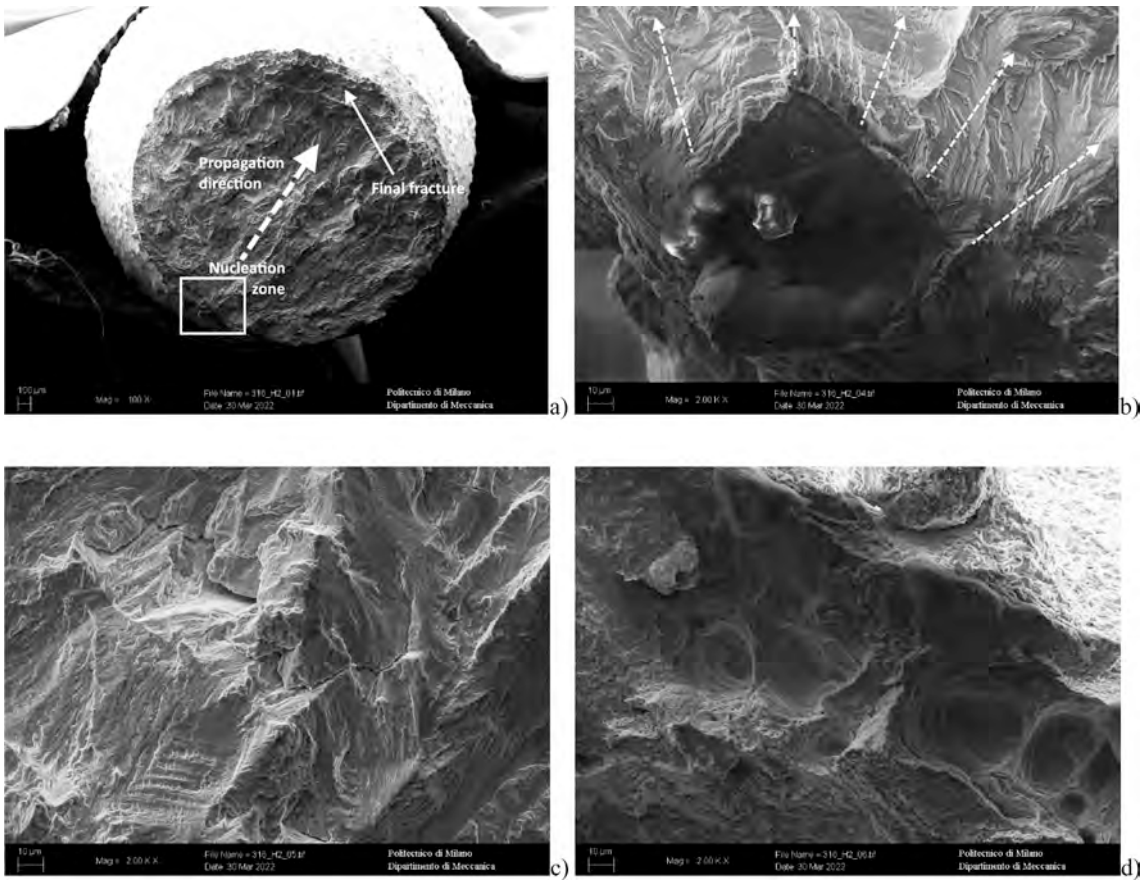

Fig. 27. Fracture surface analysis of specimen HCF2 - (a) fracture surface, (b) nucleation zone characterized by the presence of an un-melted zone, (c) propagation zone, (d) final fracture.

determination becomes critical since process-induced defects cannot be avoided completely. On the other hand, the same microstructural features cannot be replicated by other manufacturing processes. According to the technical literature, the fatigue limit can be estimated as a fraction of UTS depending on the fatigue loading type. However, even though quasi-static tensile properties are less influenced by porosity, it is not possible to completely exclude a detrimental effect also on such properties. Among the mechanical parameters usually adopted to characterize a material, hardness seems the most suitable to investigate the mechanical properties of the bulk material reducing as much as possible the porosity influence. In fact, the hardness test can be done sufficiently far from defects. When a flaw is located below the tested region, the imprint shape will be irregular and hence not acceptable. So, relating the hardness to the fatigue limit seems a promising way to estimate a value only dependent on the microstructure. In the technical literature [25,70], the fatigue limit at $R=-1$ can be estimated as:

$$\sigma_{f0} \cong 1.6HV \tag{15}$$

where HV is the Vickers hardness.

As reported in [25], such expression is obtained approximating the fatigue limit as $\sigma_{f0} = 0.5UTS$ and the ultimate tensile strength as $UTS = 3.3HV$. Such relation is more suitable for BCC materials since the ratio between fatigue limit and UTS is generally lower than 0.5 for FCC materials.

Murakami and other authors [25,70,71] proposed Equation (16) to relate the fatigue limit, the hardness and the equivalent micro-notch length ($\sqrt{area}$) of an existing defect in [μm].

$$\Delta\sigma_w = 2\frac{a(HV+b)}{(\sqrt{area})^{1/6}} \tag{16}$$

where $\Delta\sigma_w$ is the fatigue limit stress range with $R=-1$. The constant a is equal to 1.43 and 1.56 for surface and inner defects, respectively. In [25], the constant b is equal to 120. More recently, some authors [72,73] proposed the constant b equal to 75 for aluminum alloys.

When a different load ratio is applied, Equation (16) is modified as reported in Equation (17).

$$\Delta\sigma_w(R) = 2\frac{a(HV+b)}{(\sqrt{area})^{1/6}}\left(\frac{1-R}{2}\right)^{\alpha} \tag{17}$$

α is a coefficient correlated to the hardness as shown in Equation (18).

$$\alpha = 0.226 + 10^{-4}HV \tag{18}$$

This model was tested considering many experimental data with a good agreement (±15 %) [25].

Considering the previous expressions, the authors calculated the theoretical (defect-free) fatigue limit replacing in Equation (17) the equivalent micro-notch defect length $\sqrt{area}$ with the El-Haddad intrinsic flaw calculated according to Equation (6). The combination of Equations (17) and (6) resulted in:

$$\Delta\sigma_w(R) = 2\frac{a(HV+b)}{\left[\frac{1}{\pi}\left(\frac{\Delta K_{th,LC}(R)}{Y\Delta\sigma_w(R)}\right)^2 10^6\right]^{1/6}}\left(\frac{1-R}{2}\right)^{\alpha} \tag{19}$$

To find the fatigue limit $\Delta\sigma_w(R)$, Equation (19) can be rearranged as shown in Equation (20).

$$\Delta\sigma_w(R) = \left[2\frac{a(HV+b)\pi^{1/6}Y^{1/3}}{10\left(\Delta K_{th,LC}(R)\right)^{1/3}}\left(\frac{1-R}{2}\right)^{\alpha}\right]^{3/2} \tag{20}$$

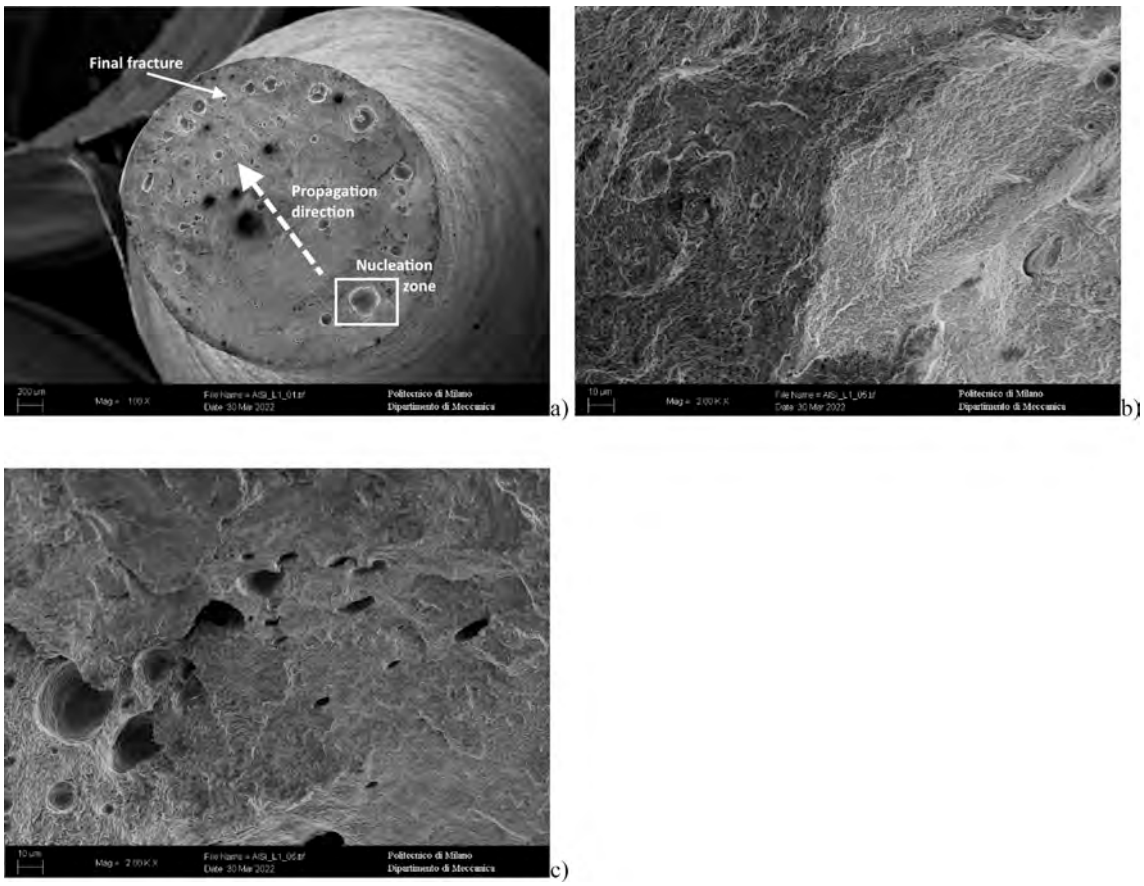

Fig. 28. Fracture surface analysis of specimen LCF1- (a) fracture surface, (b) propagation zone, (c) fracture zone. Macro- and micro-porosity is clearly visible.

Finally, the maximum fatigue stress can be calculated with Equation (21):

$$\sigma_{w,max}(R) = \sigma_{f0}(R) = \frac{\Delta\sigma_w(R)}{(1-R)} \tag{21}$$

The estimated theoretical fatigue limits for the investigated alloys are summarized in Table 8.

Regarding additively-manufactured samples, the identification of the theoretical fatigue limit by experimental tests is quite complicated since it would require polished and defect-free specimens. Moreover, being the microstructure strongly affected by the production technique, it is almost impossible to replicate it using conventional casting methods. So, the unique possibility to determine experimentally the theoretical fatigue limit is the complete removal of the AM process-induced defects. A very effective solution in closing pores is the Hot Isostatic Pressing (HIP) technique. Nevertheless, the presence of high temperatures strongly modifies both the microstructure and the mechanical properties. Laser remelting is an alternative method to reduce the defects content significantly. This technique requires the re-scanning of each powder layer twice before going to the next one. However, it involves microstructural modifications which result in different mechanical properties compared to those associated with the standard AM technique. Since these methods are very expensive, the authors decided to compare the estimated fatigue limits with the experimental data found in the scientific literature. Regarding AISI 316L, Rivolta et al. [63] reported many data for fatigue tests on wrought smooth specimens with load ratio $R = -1$. The reported σ_{f0}/UTS ratio ranges between 0.35 and 0.54. Such values can be converted to the load ratio $R = 0$ with the Goodman-Smith relation obtaining the interval from 0.52 to 0.70. So, the values presented in Table 8 are compatible with the literature data.

Regarding AlSi10Mg, many data about cast aluminum alloys are present in the technical literature [64]. The reported σ_{f0}/UTS ratio interval, converted to $R = 0$, ranges between 0.25 and 0.59. Considering only the data of the investment cast and HIP conditions (the ones with the highest quality), the interval becomes narrower, i.e. 0.44–0.59. Considering such data, the values shown in Table 8 are compatible with the available technical literature.

Finally, the limit curves for non-propagating cracks calculated according to Equations (9), (10) and (12), are compared in Fig. 19 for the investigated alloys.

In the following analysis, Equation (12) is taken as the reference model for the limit curve of non-propagating cracks. The surface roughness and the surface/inner defects can be converted into equivalent micro-notches considering the Murakami's approach [25]. Their length influences the limit curves as reported in Fig. 20.

Some of the broken fatigue specimens were observed by SEM, as shown in Section 7. The crack nucleations occurred at the surface because of the roughness notch effect or the combined effect of roughness and near-surface pores. According to the Murakami's approach [25], all the defects were converted into equivalent micro-notches. Considering surface roughness as a shallow defect, its conversion can be calculated as $\sqrt{10}R_v$. For surface and inner defects, the same conversion is done considering the $\sqrt{area}$ parameter, as shown in Fig. 21. The equivalent micro-notch lengths are summarized in Table 9.

The broken fatigue specimens summarized in Table 9 were analysed using the K-T diagram referred to the corresponding material, as shown in Fig. 22.

All the broken fatigue specimens lie in the propagating crack region if compared to the corresponding limit curves. The El-Haddad limit curve is confirmed non-conservative since some of the broken fatigue samples would fall into the safe zone.

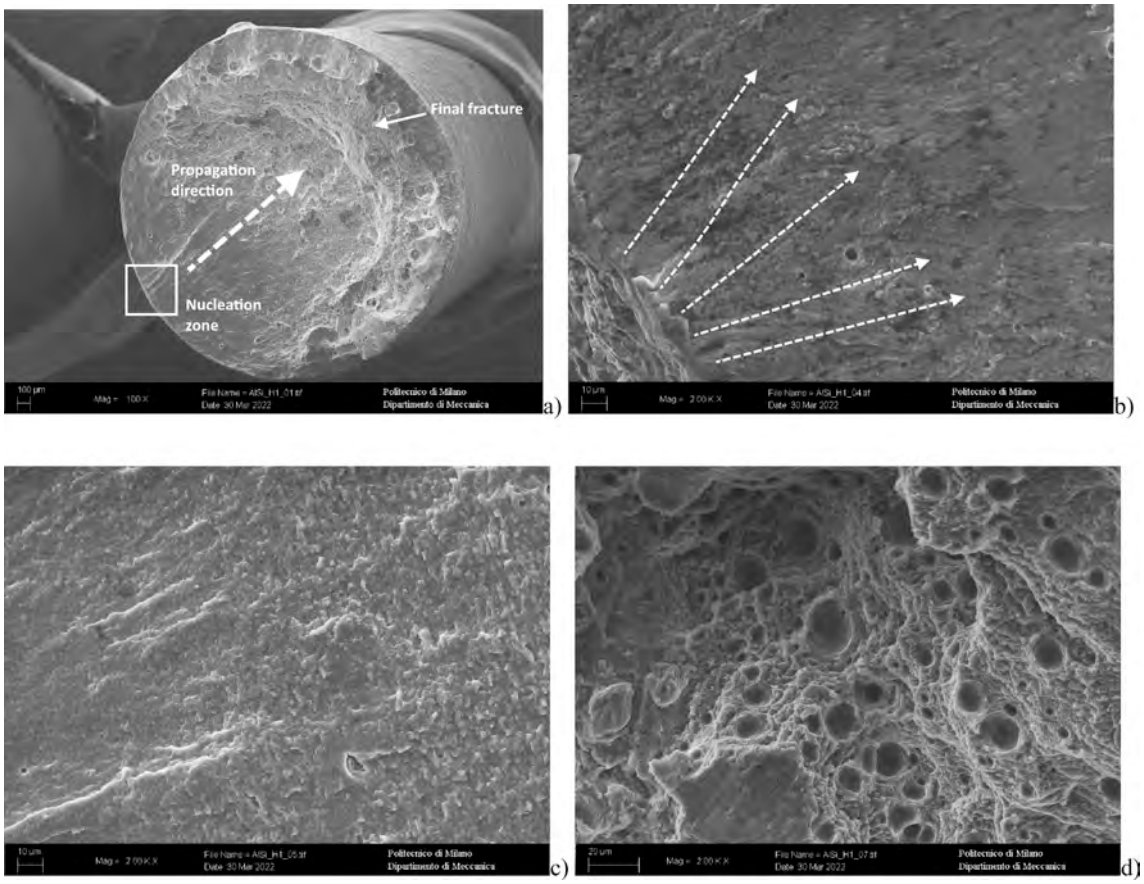

Fig. 29. Fracture surface analysis of specimen HCF1 - (a) fracture surface, (b) nucleation zone, (c) propagation zone, (d) final fracture. Macro- and micro-porosity is clearly visible.

6. Low-cycle-fatigue (LCF)

Both the tested materials showed hysteresis curves. As shown in Fig. 23, each cyclic curve was fitted by the Ramberg-Osgood (R-O) model reported in Equation (22).

$$\varepsilon_a = \varepsilon_{ae} + \varepsilon_{ap} = \frac{\sigma_a}{E} + \left(\frac{\sigma_a}{K}\right)^{\frac{1}{n}} \tag{22}$$

where ε_a is the total strain amplitude, ε_{ae} and ε_{ap} are the elastic and plastic portions of the total strain amplitude, σ_a is the stress amplitude, E is the elastic modulus, K and n are material constants. The R-O parameters are reported in Table 10.

The stabilized curves show a softening behavior for both the materials. LCF tests were carried out until rupture and the number of cycles at failure, N_f, was recorded in each test. Then, the LCF and HCF data were used to determine the coefficient of the modified Basquin-Coffin-Manson (BCM) relation shown in Equation (23).

$$\varepsilon_a = \frac{\Delta\varepsilon_a}{2} = \frac{\sigma_f^{'}}{E}(2N_f)^b + \varepsilon_f^{'}(2N_f)^c + \varepsilon_{fatigue} \tag{23}$$

$\varepsilon_f^{'}$ is the fatigue ductility coefficient, $\sigma_f^{'}$ is the fatigue strength coefficient, $2N_f$ is the number of reversals to failure (N_f is the number of cycles to failure) b is the fatigue strength exponent, c is the fatigue ductility exponent and $\varepsilon_{fatigue}$ is the strain associated to the fatigue limits reported in Table 6. Since the HCF tests were carried out at a different load ratio ($R = 0$), the fatigue limits were converted at load ratio $R = -1$ by the Goodman-Smith relation. Since the HCF limits lie in the elastic field, the strains associated to the fatigue limits at load ratio $R = -1$ were obtained with Equation (24):

$$\varepsilon_{fatigue} = \frac{\sigma_f(R=-1)}{E} \tag{24}$$

where $\sigma_f(R=-1)$ is the fatigue limit converted at load ratio $R = -1$ by the Goodman-Smith relation and E is the material elastic modulus. Finally, the modified BCM coefficients are summarized in Table 11 and the comparison among the data and the fitting curves is shown in Fig. 24.

The comparison of the obtained results with those available in the technical literature is more complicated in the case of LCF rather than HCF. In the presence of high loads close to or above the yield strength, size and distribution of inner porosity become more and more important. In fact, Solberg et al. [9] observed that crack nucleation is mainly driven by the surface condition in the case of HCF. Instead, inner defects become critical in the LCF field. The inner porosity of AM parts strongly depends on the alloy and the process type and parameters. In this work, the AISI 316L porosity is really different compared to that observed in the aluminum alloy. Nevertheless, the authors carried out a large literary review to find some experimental conditions compatible with those presented in this paper.

For example, Shrestha et al. [74] tested AM AISI 316L stainless steel under symmetrical strain-control fatigue condition. YS and UTS resulted slightly higher than those presented in Table 5 (4 % and 17 %, respectively). Nevertheless, the strain amplitude corresponding to an average number of reversals to failure equal to 1000 is close to that reported in Fig. 24.

Romano et al. [75] performed strain-controlled fatigue tests on AlSi10Mg produced with different process parameters. They found YS and UTS values ranging from 225 MPa to 305 MPa and from 365 MPa to 444 MPa, respectively. Porosity ranged between 0.02 % and 0.38 %

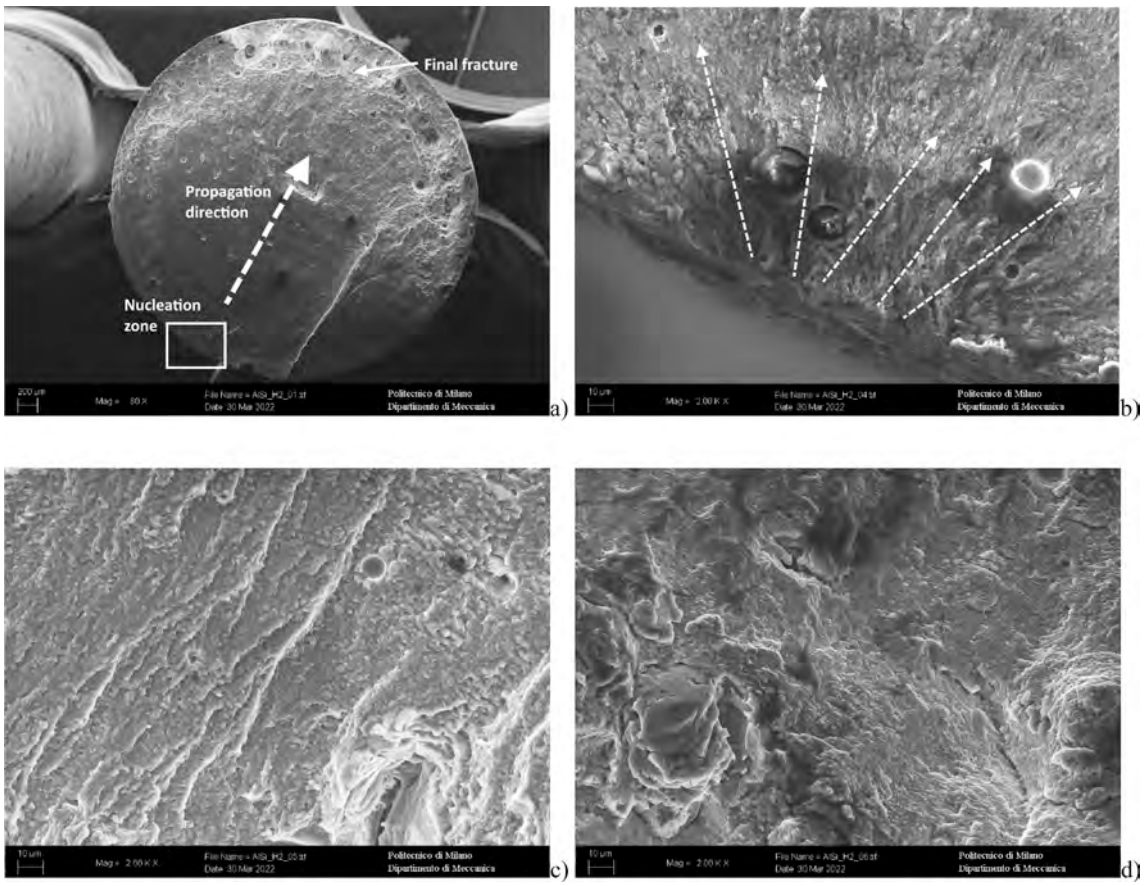

Fig. 30. Fracture surface analysis of specimen HCF2 - (a) fracture surface, (b) nucleation zone, (c) propagation zone, (d) final fracture. Macro- and micro-porosity is clearly visible.

varying the process parameters. Fatigue tests, performed with strain ratio equal to −1, resulted in a number of cycles to failure included between 10^2 and 10^7. Considering only the specimen series with the highest porosity, a strain amplitude included between $4 \bullet 10^{-3}$ and $6 \bullet 10^{-3}$ results in an average number of cycles to failure equal to 1000, similar to those reported in Fig. 24.

7. Fracture surfaces investigation

The analysis of LCF fracture surfaces was often complicated because high loads reduce the propagation areas and the typical fatigue marks are not as clear as those observed in HCF fatigue samples. Moreover, some damages were detected on the fracture surfaces, which were probably generated when the final fracture occurred. Nevertheless, crack propagation evidence was highlighted in the reported SEM micrographs. In the HCF series, instead, nucleation, propagation and final fracture zones were clear. In these samples, cracks originated on the outer surface and no multiple nucleation was observed. For both LCF and HCF specimens, the final fracture is characterized by very small dimples associated with a micro-ductile mechanism. The analyzed samples are summarized in Table 12.

7.1. AISI 316L stainless steel

See Figs. 25, 26 and 27.

7.2. AlSi10Mg alloy

See Figs. 28, 29 and 30. Due to the high loads and some damaged zones, the LCF fracture surfaces show only few features of fatigue mechanisms. The crack seems to be originated from an inner pore, as remarked in Fig. 28a.

8. Conclusions

In this experimental study, two materials, AISI 316L and AlSi10Mg were produced, tested and characterized in terms of quasi-static, high-cycle-fatigue and low-cycle-fatigue. Since AM materials are often employed for small reticular structures without any surface finishing, specimens were tested in the as-built condition. The mechanical resistance was determined by tensile and hardness tests resulting in better performance compared to conventional casting methods. Instead, the elastic modulus is similar to that of conventional alloys. Then, a comparison among the materials considering the specific YS and UTS remarked the highest performance of the AlSi10Mg alloy.

Metallographic analysis revealed the main structural features of the considered alloys. In each investigated SLMed material, melt pools were clearly visible in both longitudinal and transversal sections. A surface contour layer was present as well. In this region, a really large number of pores was present, especially in the AlSi10Mg alloy where the average defect size was higher compared to that of AISI 316L. Melt pools were composed of very fine cellular-shaped structures and elongated dendrites. Hardness values were significantly higher than those of conventionally cast products. The hardness of as-built AlSi10Mg was close to that of die-cast alloys after T6 aging treatment.

The high-cycle fatigue limit was determined using the short staircase approach according to the Dixon method. The experimental values agree with the technical literature. As expected, they are strongly influenced by defects and surface condition. As for the static properties, the fatigue behavior was compared considering the specific fatigue

limits. Such analysis confirmed the outstanding behavior of the AlSi10Mg alloy.

In the Kitagawa-Takahashi diagram, the limit curves for non-propagating cracks were determined for each material considering the total equivalent micro-notch of both the surface roughness and surface/inner defects. The El-Haddad approach demonstrated non-conservative, as already observed in the literature. Instead, when the limit curve associated to the total equivalent micro-notch of both the surface roughness and killer defect is considered, the specimen failure is justified.

Regarding the low-cycle fatigue, both the materials were characterized by an appreciable softening behavior. Successively, a modified Basquin-Coffin-Manson equation was employed to fit both the LCF and HCF data.

The analysis of LCF and HCF fracture surfaces revealed that crack nucleation mainly occurs close to the surface because of both poor surface quality and presence of near-surface defects. As expected, because of the FCC lattice, the final rupture of all the investigated alloys was characterized by micro-dimples, confirming the presence of a ductile behavior.

The analysis of the fracture surfaces revealed that most of the cracks nucleated from surface or sub-surface defects. This prevalent behavior is justified by the greater severity of surface defects which are associated to the highest Y coefficient in Equation (3). In only one case, the AlSi10Mg LCF1 specimen of Fig. 28, the fatigue failure originated from an inner pore. In this case, despite the lower Y value adopted for inner defects, the presence of a really large size parameter $\sqrt{area}$ was predominant in defining it as the most critical defect in terms of stress-intensity factor.

Funding source

This research did not receive any specific grant from funding agencies in the public, commercial, or not-for-profit sectors.

CRediT authorship contribution statement

Franco Concli: Investigation, Supervision, Writing – review & editing. **Riccardo Gerosa:** Investigation, Supervision, Writing – review & editing. **Davide Panzeri:** Investigation, Writing – original draft. **Lorenzo Fraccaroli:** Investigation, Writing – original draft.

Declaration of Competing Interest

The authors declare that they have no known competing financial interests or personal relationships that could have appeared to influence the work reported in this paper.

Data availability

The data that has been used is confidential.

References

[1] Hu Y, Lin X, Li Y, Ou Y, Gao X, Zhang Q, et al. Microstructural evolution and anisotropic mechanical properties of Inconel 625 superalloy fabricated by directed energy deposition. J. Alloy. Compd. 2021;870:159426. https://doi.org/10.1016/j.jallcom.2021.159426.

[2] Marchese G, Parizia S, Rashidi M, Saboori A, Manfredi D, Ugues D, et al. The role of texturing and microstructure evolution on the tensile behavior of heat-treated inconel 625 produced via laser powder bed fusion. Mater. Sci. Eng. A 2020;769:138500. https://doi.org/10.1016/j.msea.2019.138500.

[3] Sprengel M, Ulbricht A, Evans A, Kromm A, Sommer K, Werner T, et al. Towards the optimization of post-laser powder bed fusion stress-relieve treatments of stainless steel 316L. Metall. Mater. Trans. A 2021;52:5342–56. https://doi.org/10.1007/s11661-021-06472-6.

[4] Arısoy YM, Criales LE, Özel T. Modeling and simulation of thermal field and solidification in laser powder bed fusion of nickel alloy IN625. Opt. Laser Technol. 2019;109:278–92. https://doi.org/10.1016/j.optlastec.2018.08.016.

[5] Afkhami S, Dabiri M, Alavi SH, Björk T, Salminen A. Fatigue characteristics of steels manufactured by selective laser melting. Int. J. Fatigue 2019;122:72–83. https://doi.org/10.1016/j.ijfatigue.2018.12.029.

[6] Shamsujjoha Md, Agnew SR, Fitz-Gerald JM, Moore WR, Newman TA. High strength and ductility of additively manufactured 316L stainless steel explained. Metall. Mater. Trans. A 2018;49:3011–27. https://doi.org/10.1007/s11661-018-4607-2.

[7] Charmi A, Falkenberg R, Ávila L, Mohr G, Sommer K, Ulbricht A, et al. Mechanical anisotropy of additively manufactured stainless steel 316L: An experimental and numerical study. Mater. Sci. Eng. A 2021;799:140154. https://doi.org/10.1016/j.msea.2020.140154.

[8] Ronneberg T, Davies CM, Hooper PA. Revealing relationships between porosity, microstructure and mechanical properties of laser powder bed fusion 316L stainless steel through heat treatment. Mater. Des. 2020;189:108481. https://doi.org/10.1016/j.matdes.2020.108481.

[9] Solberg K, Guan S, Razavi SMJ, Welo T, Chan KC, Berto F. Fatigue of additively manufactured 316L stainless steel: The influence of porosity and surface roughness. Fatigue Fract. Eng. Mater. Struct. 2019;42:2043–52. https://doi.org/10.1111/ffe.13077.

[10] Elangeswaran C, Cutolo A, Muralidharan GK, de Formanoir C, Berto F, Vanmeensel K, et al. Effect of post-treatments on the fatigue behaviour of 316L stainless steel manufactured by laser powder bed fusion. Int. J. Fatigue 2019;123:31–9. https://doi.org/10.1016/j.ijfatigue.2019.01.013.

[11] Andreau O, Pessard E, Koutiri I, Penot J-D, Dupuy C, Saintier N, et al. A competition between the contour and hatching zones on the high cycle fatigue behaviour of a 316L stainless steel: Analyzed using X-ray computed tomography. Mater. Sci. Eng. A 2019;757:146–59. https://doi.org/10.1016/j.msea.2019.04.101.

[12] He L, Akebono H, Kato M, Sugeta A. Fatigue life prediction method for AISI 316 stainless steel under variable-amplitude loading considering low-amplitude loading below the endurance limit in the ultrahigh cycle regime. Int. J. Fatigue 2017;101:18–26. https://doi.org/10.1016/j.ijfatigue.2017.04.006.

[13] Zhang H, Zhu H, Qi T, Hu Z, Zeng X. Selective laser melting of high strength Al–Cu–Mg alloys: Processing, microstructure and mechanical properties. Mater. Sci. Eng. A 2016;656:47–54. https://doi.org/10.1016/j.msea.2015.12.101.

[14] Montero-Sistiaga ML, Mertens R, Vrancken B, Wang X, Van Hooreweder B, Kruth J-P, et al. Changing the alloy composition of Al7075 for better processability by selective laser melting. J. Mater. Process. Technol. 2016;238:437–45. https://doi.org/10.1016/j.jmatprotec.2016.08.003.

[15] Brandl E, Heckenberger U, Holzinger V, Buchbinder D. Additive manufactured AlSi10Mg samples using Selective Laser Melting (SLM): Microstructure, high cycle fatigue, and fracture behavior. Mater. Des. 2012;34:159–69. https://doi.org/10.1016/j.matdes.2011.07.067.

[16] Thijs L, Kempen K, Kruth J-P, Van Humbeeck J. Fine-structured aluminium products with controllable texture by selective laser melting of pre-alloyed AlSi10Mg powder. Acta Mater. 2013;61:1809–19. https://doi.org/10.1016/j.actamat.2012.11.052.

[17] Kimura T, Nakamoto T. Microstructures and mechanical properties of A356 (AlSi7Mg0.3) aluminum alloy fabricated by selective laser melting. Mater. Des. 2016;89:1294–301. https://doi.org/10.1016/j.matdes.2015.10.065.

[18] Fousová M, Dvorský D, Michalcová A, Vojtěch D. Changes in the microstructure and mechanical properties of additively manufactured AlSi10Mg alloy after exposure to elevated temperatures. Mater Charact 2018;137:119–26. https://doi.org/10.1016/j.matchar.2018.01.028.

[19] Casati R, Vedani M. Aging response of an A357 Al alloy processed by selective laser melting. Adv. Eng. Mater. 2019;21:1800406. https://doi.org/10.1002/adem.201800406.

[20] Yang KV, Rometsch P, Davies CHJ, Huang A, Wu X. Effect of heat treatment on the microstructure and anisotropy in mechanical properties of A357 alloy produced by selective laser melting. Mater. Des. 2018;154:275–90. https://doi.org/10.1016/j.matdes.2018.05.026.

[21] Tang M, Pistorius PC. Oxides, porosity and fatigue performance of AlSi10Mg parts produced by selective laser melting. Int. J. Fatigue 2017;94:192–201. https://doi.org/10.1016/j.ijfatigue.2016.06.002.

[22] Beretta S, Gargourimotlagh M, Foletti S, du Plessis A, Riccio M. Fatigue strength assessment of "as built" AlSi10Mg manufactured by SLM with different build orientations. Int. J. Fatigue 2020;139:105737. https://doi.org/10.1016/j.ijfatigue.2020.105737.

[23] Shi Y, Yang K, Kairy SK, Palm F, Wu X, Rometsch PA. Effect of platform temperature on the porosity, microstructure and mechanical properties of an Al–Mg–Sc–Zr alloy fabricated by selective laser melting. Mater. Sci. Eng. A 2018;732:41–52. https://doi.org/10.1016/j.msea.2018.06.049.

[24] BSI Standards, ISO 21920–2:2022: Geometrical product specifications (GPS) — Surface texture: Profile - Part 2: Terms, definitions and surface texture parameters, (2022).

[25] Y. Murakami, Metal Fatigue: Effects of Small Defects and Nonmetallic Inclusions., Elsevier, 2002. https://doi.org/10.1016/B978-0-08-044064-4.X5000-2.

[26] ASTM International, E466 - 21: Standard Practice for Conducting Force Controlled Constant Amplitude Axial Fatigue Tests of Metallic Materials 2021 10.1520/E0466-21.

[27] Maccioni L, Fraccaroli L, Borgianni Y, Concli F. High-cycle-fatigue characterization of an additive manufacturing 17–4 PH stainless steel. Key Eng. Mater. 2021;877:49–54. https://doi.org/10.4028/www.scientific.net/KEM.877.49.

[28] Concli F, Fraccaroli L, Nalli F, Cortese L. High and low-cycle-fatigue properties of 17–4 PH manufactured via selective laser melting in as-built, machined and hipped

conditions. Progress in Additive Manufacturing 2022;7:99–109. https://doi.org/10.1007/s40964-021-00217-y.
[29] Jian ZM, Qian GA, Paolino DS, Tridello A, Berto F, Hong YS. Crack initiation behavior and fatigue performance up to very-high-cycle regime of AlSi10Mg fabricated by selective laser melting with two powder sizes. Int. J. Fatigue 2021; 143:106013. https://doi.org/10.1016/j.ijfatigue.2020.106013.
[30] Zhang J, Li J, Wu S, Zhang W, Sun J, Qian G. High-cycle and very-high-cycle fatigue lifetime prediction of additively manufactured AlSi10Mg via crystal plasticity finite element method. Int. J. Fatigue 2022;155:106577. https://doi.org/10.1016/j.ijfatigue.2021.106577.
[31] Qian G, Jian Z, Qian Y, Pan X, Ma X, Hong Y. Very-high-cycle fatigue behavior of AlSi10Mg manufactured by selective laser melting: Effect of build orientation and mean stress. Int. J. Fatigue 2020;138:105696. https://doi.org/10.1016/j.ijfatigue.2020.105696.
[32] Concli F. Austempered Ductile Iron (ADI) for gears: Contact and bending fatigue behavior. Procedia Struct. Integrity 2018;8:14–23. https://doi.org/10.1016/j.prostr.2017.12.003.
[33] Gorla C, Conrado E, Rosa F, Concli F. Contact and bending fatigue behaviour of austempered ductile iron gears. Proc Inst Mech Eng C J Mech Engineering and Science 2018;232:998–1008. https://doi.org/10.1177/0954406217695846.
[34] Gorla C, Rosa F, Conrado E, Concli F. Bending fatigue strength of case carburized and nitrided gear steels for aeronautical applications. Int. J. Appl. Eng. Res. 2017; 12:11306–22.
[35] Dixon WJ. The up-and-down method for small samples. J. Am. Stat. Assoc. 1965; 60:967–78. https://doi.org/10.1080/01621459.1965.10480843.
[36] Domfang Ngnekou JN, Nadot Y, Henaff G, Nicolai J, Kan WH, Cairney JM, et al. Fatigue properties of AlSi10Mg produced by additive layer manufacturing. Int. J. Fatigue 2019;119:160–72. https://doi.org/10.1016/j.ijfatigue.2018.09.029.
[37] El Haddad MH, Smith KN, Topper TH. Fatigue crack propagation of short cracks. J. Eng. Mater. Technol. 1979;101:42–6. https://doi.org/10.1115/1.3443647.
[38] Kitagawa H. Applicability of fracture mechanics to very small cracks or the cracks in the early stage. In: Proc. 2nd Int. Conf. on Mechanical Behaviour of Materials; 1976. p. 627–31.
[39] Tanaka K, Akiniwa Y. Resistance-curve method for predicting propagation threshold of short fatigue cracks at notches. Eng. Fract. Mech. 1988;30:863–76. https://doi.org/10.1016/0013-7944(88)90146-4.
[40] Pippan R, Berger M, Stüwe HP. The influence of crack length on fatigue crack growth in deep sharp notches. Metall. Trans. A 1987;18(3):429–35.
[41] Chapetti M. Fatigue propagation threshold of short cracks under constant amplitude loading. Int. J. Fatigue 2003;25:1319–26. https://doi.org/10.1016/S0142-1123(03)00065-3.
[42] McEvily AJ, Minakawa K. On crack closure and the notch size effect in fatigue. Eng. Fract. Mech. 1987;28:519–27. https://doi.org/10.1016/0013-7944(87)90049-X.
[43] Zerbst U, Madia M. Fracture mechanics based assessment of the fatigue strength: approach for the determination of the initial crack size. Fatigue Fract. Eng. Mater. Struct. 2015;38:1066–75. https://doi.org/10.1111/ffe.12288.
[44] Li B, Rosa LG. Prediction models of intrinsic fatigue threshold in metal alloys examined by experimental data. Int. J. Fatigue 2016;82:616–23. https://doi.org/10.1016/j.ijfatigue.2015.09.018.
[45] Pippan R, Riemelmoser FO. Modeling of fatigue crack growth: Dislocation models, in: Comprehensive structural integrity. In: Comprehensive Structural Integrity. Elsevier; 2003. p. 191–207. https://doi.org/10.1016/B0-08-043749-4/04035-0.
[46] Maierhofer J, Gänser H-P, Pippan R. Modified kitagawa-takahashi diagram accounting for finite notch depths. Int. J. Fatigue 2015;70:503–9. https://doi.org/10.1016/j.ijfatigue.2014.07.007.
[47] ASTM International, E606/E606M − 21: Standard Test Method for Strain-Controlled Fatigue Testing, 2021 10.1520/E0606_E0606M-21.
[48] Maccioni L, Rampazzo E, Nalli F, Borgianni Y, Concli F. Low-cycle-fatigue properties of a 17–4 PH stainless steel manufactured via selective laser melting. Key Eng. Mater. 2021;877:55–60. https://doi.org/10.4028/www.scientific.net/KEM.877.55.
[49] Cao L, Li J, Hu J, Liu H, Wu Y, Zhou Q. Optimization of surface roughness and dimensional accuracy in LPBF additive manufacturing. Opt. Laser Technol. 2021; 142:107246. https://doi.org/10.1016/j.optlastec.2021.107246.
[50] Cao Q, Bai Y, Zhang J, Shi Z, Fuh JYH, Wang H. Removability of 316L stainless steel cone and block support structures fabricated by Selective Laser Melting (SLM). Mater. Des. 2020;191:108691. https://doi.org/10.1016/j.matdes.2020.108691.
[51] Uzan NE, Shneck R, Yeheskel O, Frage N. Fatigue of AlSi10Mg specimens fabricated by additive manufacturing selective laser melting (AM-SLM). Mater. Sci. Eng. A 2017;704:229–37. https://doi.org/10.1016/j.msea.2017.08.027.
[52] Tridello A, Fiocchi J, Biffi CA, Rossetto M, Tuissi A, Paolino DS. Size-effects affecting the fatigue response up to 109 cycles (VHCF) of SLM AlSi10Mg specimens produced in horizontal and vertical directions. Int. J. Fatigue 2022;160:106825. https://doi.org/10.1016/j.ijfatigue.2022.106825.
[53] Tridello A, Fiocchi J, Biffi CA, Chiandussi G, Rossetto M, Tuissi A, et al. Effect of microstructure, residual stresses and building orientation on the fatigue response up to 109 cycles of an SLM AlSi10Mg alloy. Int. J. Fatigue 2020;137:105659. https://doi.org/10.1016/j.ijfatigue.2020.105659.
[54] Nguejio J, Szmytka F, Hallais S, Tanguy A, Nardone S, Godino Martinez M. Comparison of microstructure features and mechanical properties for additive manufactured and wrought nickel alloys 625. Mater. Sci. Eng. A 2019;764:138214. https://doi.org/10.1016/j.msea.2019.138214.
[55] Silva CC, de Albuquerque VHC, Miná EM, Moura EP, Tavares JMRS. Mechanical properties and microstructural characterization of aged nickel-based alloy 625 weld metal. Metall. Mater. Trans. A 2018;49:1653–73. https://doi.org/10.1007/s11661-018-4526-2.
[56] Bagherifard S, Beretta N, Monti S, Riccio M, Bandini M, Guagliano M. On the fatigue strength enhancement of additive manufactured AlSi10Mg parts by mechanical and thermal post-processing. Mater. Des. 2018;145:28–41. https://doi.org/10.1016/j.matdes.2018.02.055.
[57] Saeidi K, Gao X, Zhong Y, Shen ZJ. Hardened austenite steel with columnar sub-grain structure formed by laser melting. Mater. Sci. Eng. A 2015;625:221–9. https://doi.org/10.1016/j.msea.2014.12.018.
[58] Kurzynowski T, Gruber K, Stopyra W, Kuźnicka B, Chlebus E. Correlation between process parameters, microstructure and properties of 316 L stainless steel processed by selective laser melting. Mater. Sci. Eng. A 2018;718:64–73. https://doi.org/10.1016/j.msea.2018.01.103.
[59] Godec M, Zaefferer S, Podgornik B, Šinko M, Tchernychova E. Quantitative multiscale correlative microstructure analysis of additive manufacturing of stainless steel 316L processed by selective laser melting. Mater Charact 2020;160: 110074. https://doi.org/10.1016/j.matchar.2019.110074.
[60] Liverani E, Toschi S, Ceschini L, Fortunato A. Effect of selective laser melting (SLM) process parameters on microstructure and mechanical properties of 316L austenitic stainless steel. J. Mater. Process. Technol. 2017;249:255–63. https://doi.org/10.1016/j.jmatprotec.2017.05.042.
[61] Bartolomeu F, Buciumeanu M, Pinto E, Alves N, Carvalho O, Silva FS, et al. 316L stainless steel mechanical and tribological behavior—A comparison between selective laser melting, hot pressing and conventional casting. Addit. Manuf. 2017; 16:81–9. https://doi.org/10.1016/j.addma.2017.05.007.
[62] Liu M, Zhang Z, Breton F, Chen X-G. Investigation of the quench sensitivity of an AlSi10Mg alloy in permanent mold and high-pressure vacuum die castings. Materials 2019;12:1876. https://doi.org/10.3390/ma12111876.
[63] Rivolta B, Gerosa R, Panzeri D. Selective laser melted 316L stainless steel: Influence of surface and inner defects on fatigue behavior. Int. J. Fatigue 2023;172:107664. https://doi.org/10.1016/j.ijfatigue.2023.107664.
[64] Beretta S, Romano S. A comparison of fatigue strength sensitivity to defects for materials manufactured by AM or traditional processes. Int. J. Fatigue 2017;94: 178–91. https://doi.org/10.1016/j.ijfatigue.2016.06.020.
[65] Tabernig B, Pippan R. Determination of the length dependence of the threshold for fatigue crack propagation. Eng. Fract. Mech. 2002;69(8):899–907. https://doi.org/10.1016/S0013-7944(01)00129-1.
[66] Riemer A, Leuders S, Thöne M, Richard HA, Tröster T, Niendorf T. On the fatigue crack growth behavior in 316L stainless steel manufactured by selective laser melting. Eng. Fract. Mech. 2014;120:15–25. https://doi.org/10.1016/j.engfracmech.2014.03.008.
[67] Suryawanshi J, Prashanth KG, Ramamurty U. Mechanical behavior of selective laser melted 316L stainless steel. Mater. Sci. Eng. A 2017;696:113–21. https://doi.org/10.1016/j.msea.2017.04.058.
[68] Riemer A, Richard HA. Crack propagation in additive manufactured materials and structures. Procedia Struct. Integrity 2016;2:1229–36. https://doi.org/10.1016/j.prostr.2016.06.157.
[69] Xu Z, Liu A, Wang X. Fatigue performance and crack propagation behavior of selective laser melted AlSi10Mg in 0°, 15°, 45° and 90° building directions. Mater. Sci. Eng. A 2021;812:141141. https://doi.org/10.1016/j.msea.2021.141141.
[70] Schönbauer BM, Mayer H. Effect of small defects on the fatigue strength of martensitic stainless steels. Int. J. Fatigue 2019;127:362–75. https://doi.org/10.1016/j.ijfatigue.2019.06.021.
[71] Schönbauer BM, Yanase K, Endo M. The influence of various types of small defects on the fatigue limit of precipitation-hardened 17–4PH stainless steel. Theor. Appl. Fract. Mech. 2017;87:35–49. https://doi.org/10.1016/j.tafmec.2016.10.003.
[72] Tajiri A, Nozaki T, Uematsu Y, Kakiuchi T, Nakajima M, Nakamura Y, et al. Fatigue limit prediction of large scale cast aluminum alloy A356, Procedia. Mater. Sci. 2014;3:924–9. https://doi.org/10.1016/j.mspro.2014.06.150.
[73] Noguchi H, Morishige K, Fujii T, Kawazoe T, Hamada S. Proposal of method for estimation stress intensity factor range on small crack for light metals. In: 56th JSMS Annual Meetings; 2007. p. 137–8.
[74] Shrestha R, Simsiriwong J, Shamsaei N. Fatigue behavior of additive manufactured 316L stainless steel parts: Effects of layer orientation and surface roughness. Addit. Manuf. 2019;28:23–38. https://doi.org/10.1016/j.addma.2019.04.011.
[75] Romano S, Patriarca L, Foletti S, Beretta S. LCF behaviour and a comprehensive life prediction model for AlSi10Mg obtained by SLM. Int. J. Fatigue 2018;117:47–62. https://doi.org/10.1016/j.ijfatigue.2018.07.030.